

Jeevan Thapa

CONTROLLING AND SIZING OF THE ENERGY STORAGE SYSTEM USED FOR SMOOTHING PHOTOVOLTAIC POWER FLUCTUATIONS

Faculty of Information Technology and Communication Sciences
Examiner: Assistant Professor Kari Lappalainen
Master's Thesis
May 2024

ABSTRACT

Jeevan Thapa: Controlling and sizing of the energy storage system used for smoothing photovoltaic power fluctuations.

Master's Thesis

Tampere University

Master's Degree Programme in Electrical Engineering

May 2024

The growing presence of renewable energy sources, such as solar and wind power plants, brings about rapid expansion. However, the intermittent and unpredictable nature of solar irradiance and wind leads to fluctuating output power, posing challenges like power instability and quality issues in the grid. Few countries have already applied the Ramp Rate (RR) limit to prevent those issues. To address this, integrating Energy Storage Systems (ESSs) is essential, particularly in PV power systems, to mitigate rapid power fluctuations.

The thesis aimed to assess the impact of various smoothing strategies, with and without threshold limits, and time constants on the sizing and utilization rate of ESSs. A key novelty was the utilization of smoothing strategies like Moving Average (MA) and Low Pass Filter (LPF) with threshold limits, where the algorithm operated only when the RR in the grid-fed power exceeded the specified threshold limit. Simulation work conducted in MATLAB focused on controlling and smoothing fluctuations in PV output power, with measurements taken at the Finnish Solar PV Power Station Research Plant at Tampere University on June 11 and 15, 2021.

It was found that the primary factor influencing the size of the ESS between the MA and LPF was the relative energy capacity. For both days, the required relative energy capacity for LPF exceeded that of MA by 67.97% and 83.42%, respectively. It was observed that as the threshold limit increased, there was a decrease in both the required relative energy capacity and the utilization rate. Similarly, other findings indicated that the required energy capacity and relative power capacity in general without the threshold limit were lower compared to all the threshold limits. The utilization rate without the threshold limit was lower compared to those below the threshold limit (≤ 2 %/min and ≤ 4 %/min). However, the utilization rate without the threshold limit was higher compared to those above the threshold limit (> 2 %/min and > 4 %/min). The final findings indicated that for MA, relative energy capacity played a more significant role in determining ESS sizing. However, for LPF, shorter, intermediate, and longer time constants had minimal impact on the relative energy capacity, relative power capacity, and utilization rate.

Keywords and terms: photovoltaic power, energy storage systems, threshold limit, power fluctuations, controlling strategies, moving average, low pass filter

The originality of this thesis has been checked using the Turnitin OriginalityCheck service.

PREFACE

This Master's thesis was conducted for the Faculty of Information Technology and Communication Sciences, Electrical Engineering Unit of Tampere University. The chosen topic aligns closely with my interests and was recommended by Assistant Professor Kari Lappalainen, who also served as the thesis examiner.

As I stand on the verge of concluding my Master's degree journey, I find myself reflecting upon the infinite experiences, challenges, and discoveries that have shaped the direction of this academic endeavor. This thesis represents the conclusion of months of rigorous research, critical analysis, and firm determination.

Starting this journey has been a personal and academic experience. It would not have been possible without the invaluable guidance, support, and encouragement of my thesis advisor, Kari Lappalainen. His expertise, mentorship, and constructive feedback have been influential in refining the focus of my research and maintaining the quality of the work. I would also like to thank my friend Vikas Mohan Dixit for helping me while writing the thesis.

Undertaking a Master's thesis is no small achievement, and this accomplishment would not have been possible without the firm support of my friends and family. Their understanding, patience, and encouragement have been a constant source of strength throughout this academic journey.

I try to present a comprehensive exploration of the controlling and sizing of the energy storage systems used for smoothing photovoltaic power fluctuations. It is my aspiration that this research contributes to the existing body of knowledge in the field and ignites further inquiry among scholars and practitioners.

May this thesis stand as evidence of the pursuit of knowledge, the spirit of inquiry, and the boundless possibilities that lie ahead in the field of electrical engineering.

Tampere, Finland, May 2024

Jeevan Thapa

Jeevan.thapa@tuni.fi

CONTENTS

1	INTRODUCTION	1
2	PHOTOVOLTAIC POWER SYSTEMS	3
2.1	Working principle of PV cells and doping of the intrinsic semiconductor.....	3
2.2	Characteristics curves and efficiency of PV cells	7
2.3	Global irradiance and its effects on PV power fluctuations.....	10
3	ENERGY STORAGE SYSTEMS.....	12
3.1	Fundamentals of energy storage and its applications.....	12
3.2	Various energy storage technologies with their characteristics	15
3.2.1	Pumped Hydroelectric Storage	16
3.2.2	Compressed air energy storage	17
3.2.3	Flywheel energy storage	17
3.2.4	Battery energy storage.....	18
3.2.5	Supercapacitor.....	19
3.2.6	Superconducting magnetic energy storage.....	20
3.2.7	Hydrogen storage and fuel cell	20
3.2.8	Solar fuels	21
3.2.9	Thermal energy storage.....	22
3.3	Integration of ESSs with PV power plants.....	23
3.4	Control strategies and their impact on ESS sizing	23
4	MEASUREMENTS AND MODELING.....	25
4.1	Measurements	25
4.2	Modeling of energy storage systems.....	25
5	RESULTS AND DISCUSSION.....	28
5.1	Sizing of the ESSs with two different smoothing strategies without using the threshold limit.....	28
5.2	Sizing of the ESSs with different threshold limits and without threshold limit	30
5.3	Sizing of the ESSs with three different time constants.....	37
5.4	Discussion	40
6	Conclusion	42
	References	44
	Appendix 1: MA based control algorithm with threshold limit	49

LIST OF FIGURES

Figure 2.1. The energy band diagram of a semiconductor	4
Figure 2.2. Crystal lattice structure of n-type silicon doped with donors phosphorus	5
Figure 2.3. Crystal lattice structure of p-type silicon doped with acceptors boron	6
Figure 2.4. Illustration of the p-n junction without an external voltage source.....	7
Figure 2.5. I-V and P-V characteristics curve of a PV cell at irradiance (1 kW/m ²) and cell temperature (25 °C).....	7
Figure 2.6. I-V characteristics curve of a PV cell at varying irradiance and cell temperature (25 °C).....	8
Figure 2.7. I-V characteristics curve of a PV cell at irradiance (1 kW/m ²) and varying cell temperature	9
Figure 2.8. The best research cell efficiencies for different cells and technologies throughout the different years.....	10
Figure 2.9. Measured global irradiance on June 11, 2021, with fast-moving clouds....	11
Figure 3.1. Load leveling and peak shaving using an ESS technology	13
Figure 3.2. Employing an ESS to smooth out power fluctuations in a 3.23 kW PV Power plant	14
Figure 3.3. Integration of an ESS with a PV power plant to supply controlled power into the grid.....	15
Figure 3.4. Categorization of ESS technologies based on the form of energy stored ...	16
Figure 5.1. Power of the 3.23 kW PV string and smoothed grid power with MA and LPF strategies for 11.06.2021 and 15.06.2021	29
Figure 5.2. Maximum observed RR in the grid power as a function of threshold limits for 11.06.2021 (left) and 15.06.2021 (right).....	35
Figure 5.3. Required relative energy capacities of the ESSs as a function of threshold limits for 11.06.2021 (left) and 15.06.2021 (right).....	35
Figure 5.4. Required relative power capacities of the ESSs as a function of threshold limits for 11.06.2021 (left) and 15.06.2021 (right).....	36
Figure 5.5. Utilization rates of the ESSs as a function of threshold limits for 11.06.2021 (left) and 15.06.2021 (right)	37
Figure 5.6. Power of the 3.23 kW PV string and smoothed grid power with 3 different time constants using MA strategy for 11.06.2021 and 15.06.2021	39

LIST OF SYMBOLS AND ABBREVIATIONS

Abbreviations

AFC	Alkaline Fuel Cell
AM	Air Mass Number
BES	Battery Energy Storage
BESS	Battery Energy Storage System
CAES	Compressed Air Energy Storage
DC	Direct Current
DMFC	Direct Methanol Fuel Cell
ES	Energy Storage
ESS	Energy Storage System
EXS	Exponential Smoothing
FES	Flywheel Energy Storage
LAES	Liquid Air Energy Storage
Li-ion	Lithium-ion
LPF	Low-pass Filter
MA	Moving Average
MCFC	Molten Carbonate Fuel Cell
MPP	Maximum Power Point
MPPT	Maximum Power Point Tracker
NaS	Sodium Sulfur
NiCd	Nickel Cadmium
OC	Open-circuit
PAFC	Phosphoric Acid Fuel Cell
PCMs	Phase Change Materials
Pd	Palladium
PEMFC	Proton Exchange Membrane Fuel Cell
PHS	Pumped Hydroelectric Storage
PV	Photovoltaic
Re	Rhenium

RR	Ramp Rate
Ru	Ruthenium
SC	Short-circuit
Si	Silicon
SMES	Super Magnetic Energy Storage
SOFC	Solid Oxide Fuel Cell
STC	Standard Test Conditions
TES	Thermal Energy Storage

Symbols

E_A	Energy of an acceptor electron	eV
E_D	Energy of the donor electron	eV
E_{ESS}	Amount of energy stored in an energy storage system	J
E_G	Band gap energy	eV
G_{ex}	Total extraterrestrial irradiation	W/m ²
G_H	Global irradiance on the surface of the Earth	W/m ²
I_{sc}	Short-circuit current	A
P_{ESS}	Power of an energy storage system	W
$P_{grid,LPF}$	Grid feed-in power with LPF	W
$P_{grid,MA}$	Grid feed-in power with MA	W
P_{grid}	Grid feed-in power	W
P_{MPP}	Maximum power point power	W
P_{nom}	Nominal power of a photovoltaic power plant	W
P_{PV}	Power of a photovoltaic power plant	W
$P_{threshold_limit}$	Maximum power ramp rate for a specified threshold limit	W/s
t_1	Beginning time of the discharging period for the energy storage system	s
t_2	End time of the discharging period for the energy storage system	s
T_s	Sampling time	s
V_D	Built-in voltage	V
V_{oc}	Open-circuit voltage	V
τ_{LPF}	Time constant for LPF	s
τ_{MA}	Time constant for MA	s
I	Current	A
i	First time step	-
j	Second time step	-
P	Power	W
s	Laplace-variable	-
V	Voltage	V

1 INTRODUCTION

Photovoltaic (PV) power plants are producing more electricity, and by 2050, they will grow to be the largest source of power generation. It is predicted that almost 70 % of the electricity generation will come from solar PV and wind power plants. The total installed capacity of the solar PV power plant will be 20-fold by 2050 [1]. Due to the unpredictable and intermittent nature of solar irradiance, there are remarkable fluctuations in PV output power [2]. In about 20 seconds, the output power of the PV plant has ramped up or down ± 90 % of its rated capacity [3]. As more PV power plants are integrated into the grid, the amount of inertia in the grid reduces [4]. The combined impact of inertia and rapid power fluctuations in the electric grid leads to significant challenges in power quality and stability, such as reverse power flow and variations in voltage and frequency [5].

Electrical grid regulations have been implemented in a few nations to regulate the rate at which power ramps are introduced into utility grids [6]. To mitigate the influence of high ramp rates (RR) on the utility grid, the Puerto Rico Electric Power Authority (PREPA) has established a limit of 10 %/min for PV plants in terms of their rated capacity [7]. Similarly, Denmark has introduced a maximum power RR limit of 100 kW/s [8]. The RR limit is expressed as the percentage of the rated capacity over a time interval in minutes. Energy storage systems (ESSs) are one strategy for reducing the fluctuations of PV output power and maintaining compliance with the RR limit. The IEA anticipates that installed storage capacity on a utility-scale will rise dramatically globally in the coming years [9], [10]. Different controlling or smoothing strategies have already been used to find the size of the ESS and smooth out the rapid power fluctuations in the PV output power [11], [12], [13], [14], [15]. Moving average (MA) and low pass filter (LPF) are the controlling strategies that are applied in this thesis. These smoothing strategies without using the threshold limits have already been applied in earlier studies. The earlier results show that MA and LPF have issues like memory effects and over smoothing, which increase the size of the ESS capacity and decrease the life span [16]. Therefore, MA and LPF are used in this thesis with a new approach through the introduction of threshold limits. Threshold limits are expressed as a percentage of the RR limit in this thesis. This indicates that the MA and LPF are activated solely when the RR in the power supplied to the grid equals or exceeds the threshold limit. This approach helps to minimize over smoothing during the period when the RR is already within the threshold limit. This thesis aims to control and determine the ESS sizing requirements to address the rapid fluctuations in PV power. The research questions for this thesis are mentioned below.

- a. How do the different smoothing strategies affect the size of the ESS?

- b. How is the size of the ESSs different with and without using the threshold limits?
- c. How is the size of the ESSs different with different time constants?

MATLAB is a simulation tool that is used in this thesis to simulate the different cases for different smoothing strategies, threshold limits, and time constants. Chapter 2 contains an introduction to PV power systems, including the working principle, characteristic curves, and efficiency of PV cells. Chapter 3 delves into the fundamentals of ESSs, exploring their various types, characteristics, and applications. Additionally, it offers insight into integrating ESSs with PV power plants, discussing different control strategies and their effects on ESS sizing. Chapter 4 includes the measurements and modeling of the ESSs that are used for simulation. Chapter 5 presents the results and discussion of the simulations, and finally, Chapter 6 provides the conclusion.

2 PHOTOVOLTAIC POWER SYSTEMS

This chapter is about the fundamental concepts of PV cells that are used in PV systems. The increasing global demand for sustainable and renewable energy sources has prompted a paradigm shift towards exploring innovative technologies that can harness the abundant and inexhaustible power of the sun. Among these technologies, PV systems have emerged as a key player in the search for clean and sustainable energy. The conversion of sunlight into electricity through the photovoltaic effect has opened new opportunities for addressing the challenges posed by traditional energy resources, including environmental pollution and the depletion of finite resources [17].

The average irradiance at the outer atmospheric region surrounding the Earth is $1367 \pm 2 \text{ W/m}^2$ as solar radiation is scattered uniformly in all directions, and it is called a solar constant. Additionally, Earth rotates elliptically around the Sun around its orbit; hence, irradiance varies throughout the year, obtaining a maximum value of 1414 W/m^2 and a minimum value of 1322 W/m^2 . Solar radiation is weakened by reflection, absorption, and scattering as it travels through the atmosphere of the Earth. As a result, total extraterrestrial irradiation (G_{ex}) is greater than global irradiance (G_{H}) on the surface of the Earth [18].

In regions with moderate climates, like Central Europe, a mean air mass (AM) of AM1.5 is typical. G_{H} , on the horizontal plane surface of the Earth, is still approximately 1 kW/m^2 for solar irradiance penetrating the atmosphere of the Earth at 90° with a clear sky. G_{H} can briefly reach 1.3 kW/m^2 on a sunny day with dispersed clouds, a phenomenon known as cloud enhancement [18].

Standard Test Conditions (STC) are a group of predefined environmental parameters under which PV cells and modules are tested to assess and compare their performance. These conditions provide a standardized basis for evaluating PV cell efficiency and output, enabling fair comparisons between different technologies and systems [19]. The STC parameters of a PV module are irradiance (1000 W/m^2), temperature (25°C), and AM (1.5). AM is directly proportional to the path length of sunlight that travels through the atmosphere surrounding the Earth [20].

2.1 Working principle of PV cells and doping of the intrinsic semiconductor

PV is a technology that utilizes PV cells to directly convert solar radiation, or insolation, into electrical power. In basic terms, a PV cell is a specialized semiconductor diode featuring a thick barrier layer. When exposed to light, it permits the direct conversion of a certain amount of photon energy that enters the cell into direct current (DC) [18]. Materials categorized as semiconductors have electrical conductivities that are higher than those of insulators but lower than those of conductors. The most commonly utilized

semiconductor material in use today is silicon (Si). Si can be formed in crystalline, polycrystalline, and amorphous forms. Silicon has been a popular choice because the absorption properties of silicon fit the solar spectrum pretty well and the manufacturing processes for silicon are highly advanced and mature [21]. The outermost shell of silicon has four valence electrons. Each silicon atom forms covalent bonds with four neighboring atoms to create a stable electron configuration, and each covalent bond consists of two valence electrons [18].

When considering the properties of semiconductors, there are mainly two main types of energy bands: valence and conduction bands. If a minimum amount of external energy is provided to the valence electrons, the weakly bound valence electrons can be released into the conduction band. Electrons are free to move in the conduction band. The empty states leave positively charged carriers of currents in the valence band known as holes, whereas the released electrons act as negatively charged carriers in the conduction band [18], [21].

Band gap energy (E_G) refers to the energy difference between the conduction and valence bands. It represents the minimum energy required to excite an electron from the valence band to the conduction band. The value E_G is the largest for the insulator, the smallest for the conductor, and in between the insulator and conductor for the semiconductor. Photons possessing adequate energy levels can excite an electron from the valence band to the conduction band by absorbing the photon. This process creates a hole in the valence band and a free electron in the conduction band [18]. The energy band diagram of a semiconductor is shown in Figure 2.1.

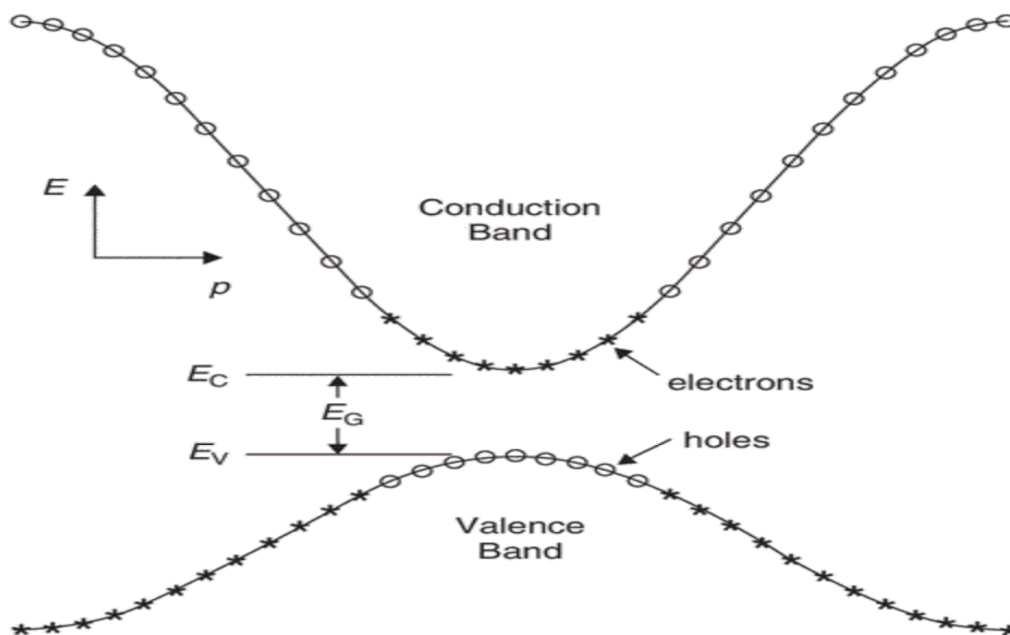


Figure 2.1. The energy band diagram of a semiconductor [21].

The intrinsic semiconductors act a lot like insulators. Hence, by introducing specific impurities, referred to as donors and acceptors, into the semiconductor, it becomes possible to regulate its conductivity [21]. As shown in Figure 2.2, one of the five valence electrons in the outermost shell of a phosphorus atom that replaces a silicon atom is unable to form a bond with any of the four adjacent atoms. Because of this, the electron can easily be liberated from the atomic nucleus, and the phosphorous atom becomes positively charged. As a result, phosphorus atoms are known as donors because they "donate" one electron to the crystal lattice. Following the band model, the energy level of the donor electron resides slightly below (E_D) the threshold of the conduction band. This indicates that the donor electron can transition to the conduction band with minimal energy gained through temperature-induced motion. The semiconductor is n-conductive because donor electrons produce conductivity through the use of negative charge carriers [18].

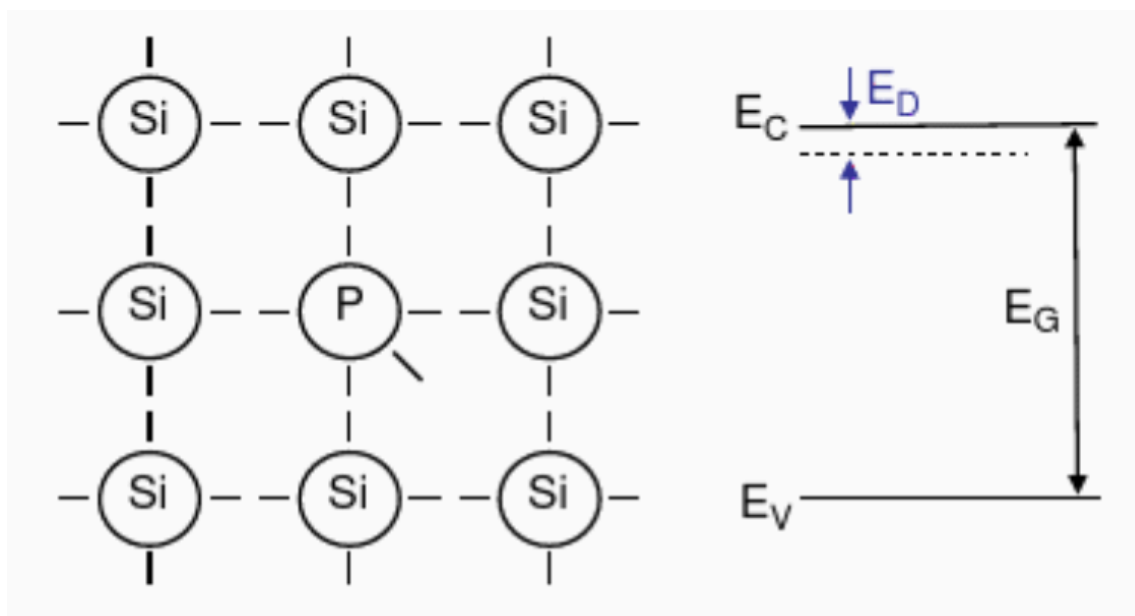


Figure 2.2. Crystal lattice structure of n-type silicon doped with donors phosphorus [18].

As shown in Figure 2.3, only three valence electrons in the outermost shell of a boron atom that substitutes a silicon atom can form bonds with three adjacent silicon atoms, and one bond is missing an electron, hence creating a hole. As a result, an electron from the valence band of a neighboring atom donates an additional electron to the boron, causing the boron atom to acquire a negative charge. As a result, boron atoms are known as acceptors because they "accept" one electron into the crystal lattice. Following the band model, the energy level of the acceptor electron resides slightly above (E_A) the threshold of the valence band. This indicates that an electron in the valence band can transition to the outermost shell of the boron with minimal energy gained through temperature-induced motion. The semiconductor exhibits p-type conductivity as acceptors generate

conductivity by creating holes in the valence band, i.e., through the use of positive charge carriers [18].

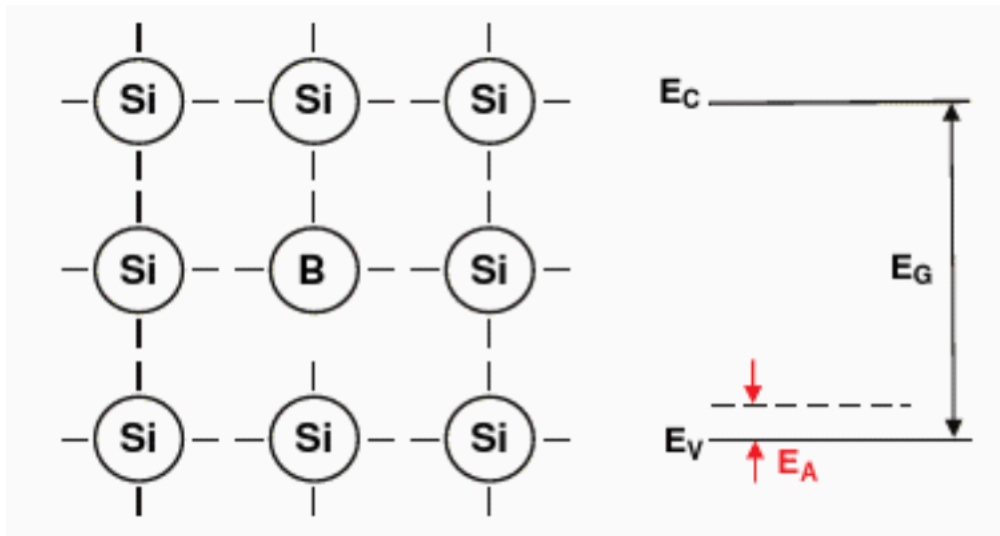


Figure 2.3. Crystal lattice structure of p-type silicon doped with acceptors boron [18].

As shown in Figure 2.4, a p-n junction is created when n-type and p-type semiconductors come into contact. Holes diffuse from the p-type region to the n-type region, while electrons diffuse from the n-type region to the p-type region due to differences in concentration between the two semiconductor types. An electrostatic potential difference is created when the impurity charges are exposed, counteracting the diffusion of the holes and electrons. In thermal equilibrium, there is no overall current flow since the diffusion of each carrier type and drift currents precisely balance. The space-charge region is the transition region between n-type and p-type semiconductors and is also referred to as the depletion area. The electric field produced by the space charges in the boundary layer hinders electron diffusion and then completely stops the diffusion process. The regions on each side of the depletion region are effectively charge-neutral if the p-type and n-type zones are thick enough. The built-in voltage (V_D), is the electrostatic potential difference that results from the junction creation [21].

When a photon hits the p-n junction of a photovoltaic cell, it generates a new electron-hole pair, releasing one electron. The electric field present in the p-n junction forces the newly generated electron and hole to move in opposing directions. The electron migrates toward the n-type region, while the hole moves toward the p-type region, as shown in Figure 2.4.

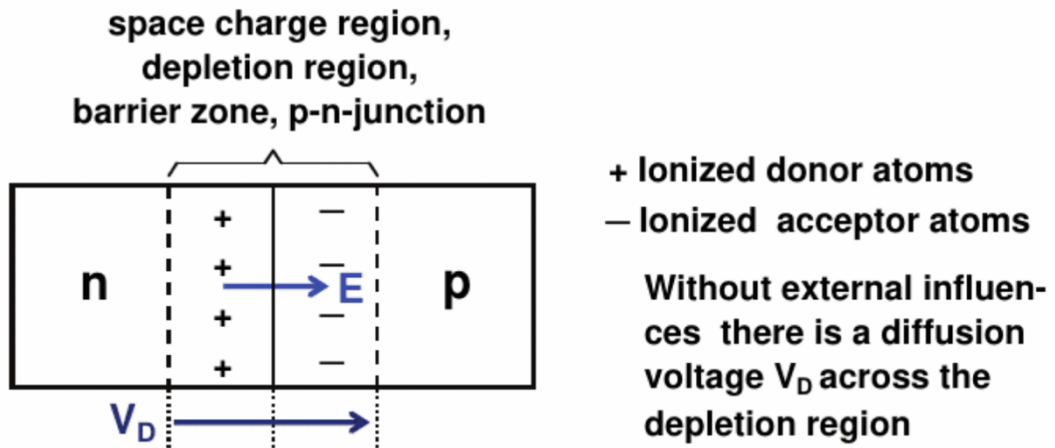


Figure 2.4. Illustration of the p-n junction without an external voltage source [18].

Additionally, the recombination of the electron and hole is obstructed by the electric field. On the opposite edges of the space charge region, electrons and holes begin to collect if the semiconductor plates are not connected to an external circuit. As soon as the semiconductor plates are linked to an external circuit, electrons and holes begin to exit the space charge region, enabling them to recombine through the external circuit. This recombination process contributes to the generation of electrical current [18].

2.2 Characteristics curves and efficiency of PV cells

Figure 2.5 shows the current-voltage ($I-V$) and power-voltage ($P-V$) characteristics curves of a PV cell. The output power of a PV cell is determined by multiplying the current and voltage. The current and voltage of a PV cell are influenced by the intensity of the irradiance and the temperature of the cell.

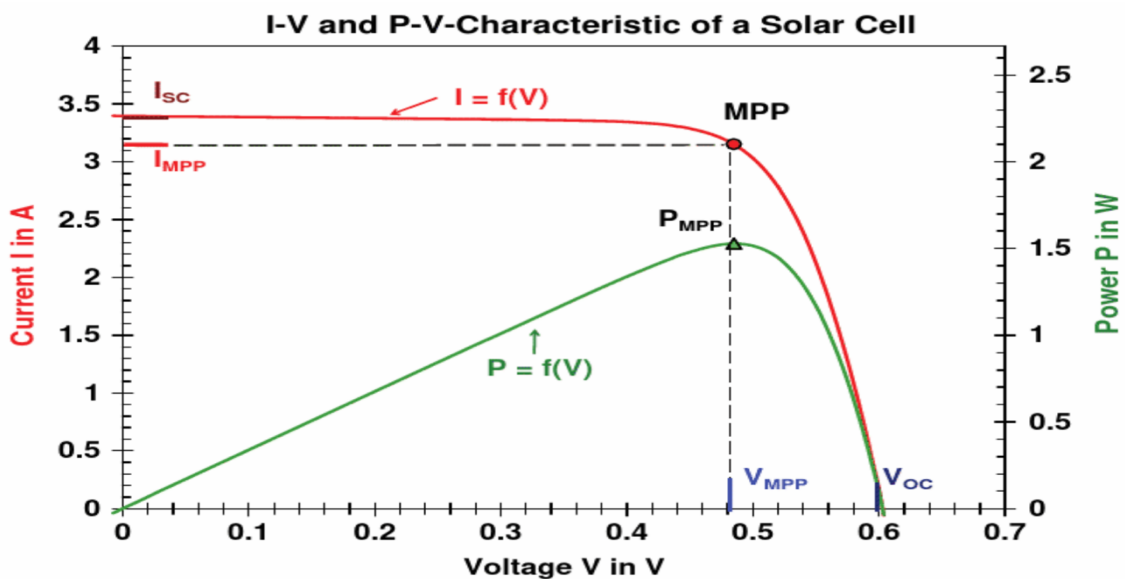


Figure 2.5. $I-V$ and $P-V$ characteristics curve of a PV cell at irradiance (1 kW/m^2) and cell temperature ($25 \text{ }^\circ\text{C}$) [18].

In Figure 2.5, it is seen that the maximum current that flows through a PV cell is called a short circuit current (I_{sc}), and the maximum voltage that is induced across the PV cell is called an open circuit voltage (V_{oc}). The point where the maximum power output occurs is referred to as the maximum power point (MPP), and the corresponding power is termed the maximum power point output (P_{MPP}). The P_{MPP} is always less than the power obtained by the multiplication of V_{oc} and I_{sc} . The main working principle regarding the output power of a PV cell is that it has to operate close to the P_{MPP} to generate the highest power possible. When the current is at its maximum (I_{sc}) value, then the voltage of the cell (V_{oc}) is zero. Likely, when the voltage (V_{oc}) is at its maximum value, the current of the cell (I_{sc}) is zero. As the current and voltage increase linearly, the power curve accelerates gradually and reaches the maximum point (P_{MPP}). After that, the power curve decelerates sharply to zero [18]. The intensity of irradiance greatly affects the I_{sc} , however, it has less effect on the V_{oc} that is depicted in Figure 2.6.

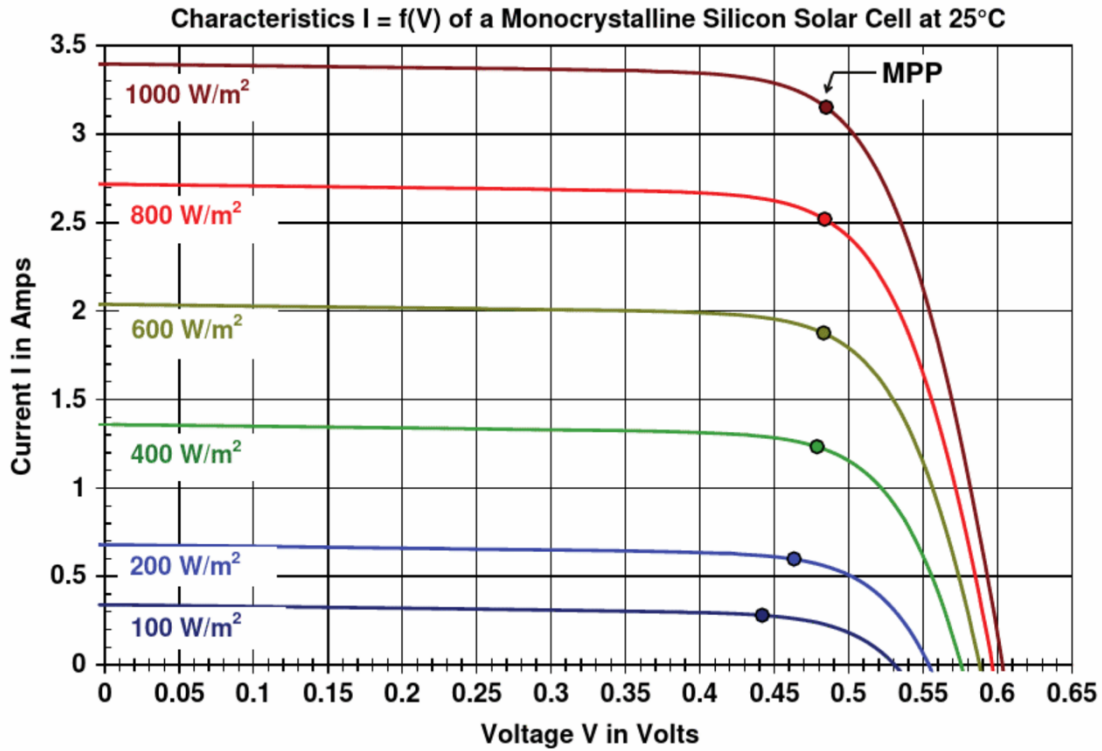


Figure 2.6. I - V characteristics curve of a PV cell at varying irradiance and cell temperature (25 °C) [18].

Figure 2.6 illustrates that as the irradiance value increases, the corresponding value of I_{sc} also increases. However, increasing irradiance slightly increases the V_{oc} . Moreover, in the beginning, the MPP voltage increases as the irradiance increases, but the MPP almost remains constant at higher values of irradiance. It is concluded that the maximum power point output (P_{MPP}) rises with an increase in solar irradiance.

Similarly, cell temperature greatly affects V_{OC} , however, it has less effect on the I_{SC} that is depicted in Figure 2.7. In Figure 2.7, it is seen that whenever the cell temperature increases, it significantly decreases the V_{OC} . However, increasing the cell temperature slightly increases the I_{SC} and makes no difference in the MPP current. As temperature increases, the band gap of a photovoltaic cell decreases, facilitating electron movement across the band gap. The voltage falls as the conductivity rises with the increased electron flow. The little increase in the I_{SC} is also a result of this phenomenon [21]. It is concluded that the P_{MPP} decreases with the increase in the cell temperature.

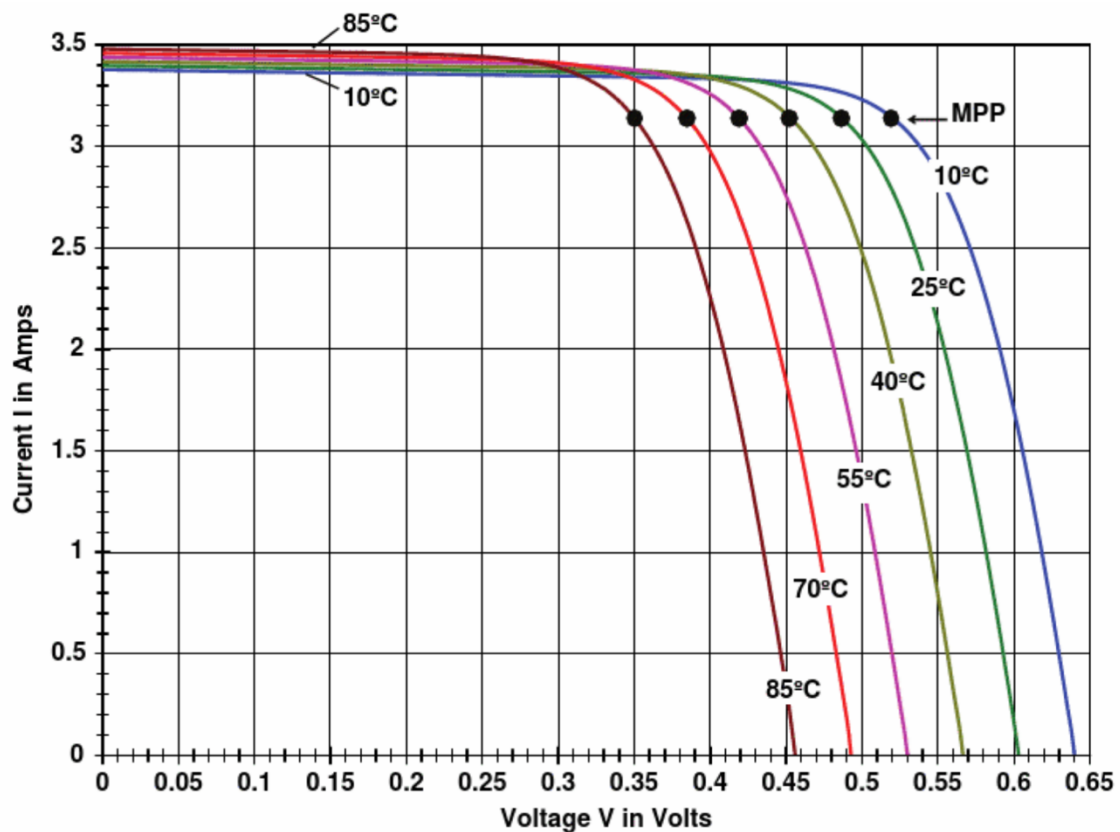


Figure 2.7. I - V characteristics curve of a PV cell at irradiance (1 kW/m^2) and varying cell temperature [18].

The efficiency of PV cells has shown a consistent increase since their invention. Currently, laboratory energy conversion efficiencies for crystalline silicon photovoltaic cells exceed 25%, while multi-crystalline cells achieve over 20%. However, commercially produced solar modules currently reach efficiencies between 18% and 22% under STC [22].

Figure 2.8 shows a chart prepared by the National Renewable Energy Laboratory indicating the highest research cell efficiencies throughout the different years.

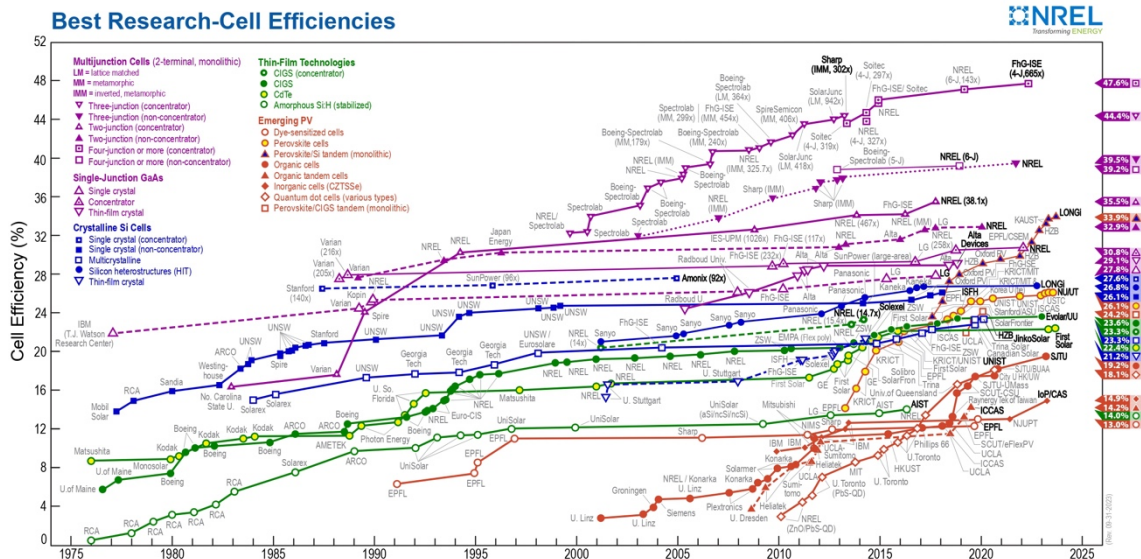


Figure 2.8. The best research cell efficiencies for different cells and technologies throughout the different years [23].

Figure 2.8 demonstrates that the efficiency of the crystalline Si cells varies from 21.2 % to 27.6 %. The single Si crystal has the highest efficiency, whereas the thin-film Si crystal has the lowest efficiency. The single-junction GaAs have an efficiency range of 27.8 % to 30.8 %. The single GaAs crystal has the highest efficiency, whereas the thin-film GaAs crystal has the lowest efficiency. For the thin film technologies, the efficiency varies from 14 % to 23.6 %. CIGS has the highest efficiency, whereas the amorphous Si:H has the minimum efficiency. The efficiency of the emerging PV ranges from 13 % to 33.9 %. Perovskite/Si tandem (monolithic) has the highest efficiency, whereas dye-sensitized cells have the lowest efficiency. Thus, it can be inferred that thin film technologies and emerging PV technologies exhibit the lowest cell efficiencies. Finally, the efficiency of multijunction cells ranges from 32.9 % to 47.6 %. Four junctions or more (concentrators) have the highest efficiency, whereas two junctions (non-concentrators) have the lowest efficiency [23].

2.3 Global irradiance and its effects on PV power fluctuations

Short-term fluctuations in global irradiance can be substantial. These fluctuations directly affect the generated power of a PV cell, and they are primarily influenced by the movement of the Sun and changes in cloud cover. The movement of the Sun leads to predictable variations in global irradiance throughout the day. During days with rapidly moving clouds, the efficiency of a PV power plant can experience significant fluctuations. Even a small cloud passing between the Sun and the PV panels can cause the generated power to

fluctuate rapidly, dropping from full capacity to near zero and then back up to full power within seconds [24]. Research indicates that these power fluctuations can reach rates as high as 70 %/min for a 9.5 MW PV power plant [3], and even more drastic fluctuations, exceeding 40 %/s, have been observed for 3.23 kW PV strings [25]. Figure 2.9 illustrates the rapid variations in global irradiance associated with these phenomena.

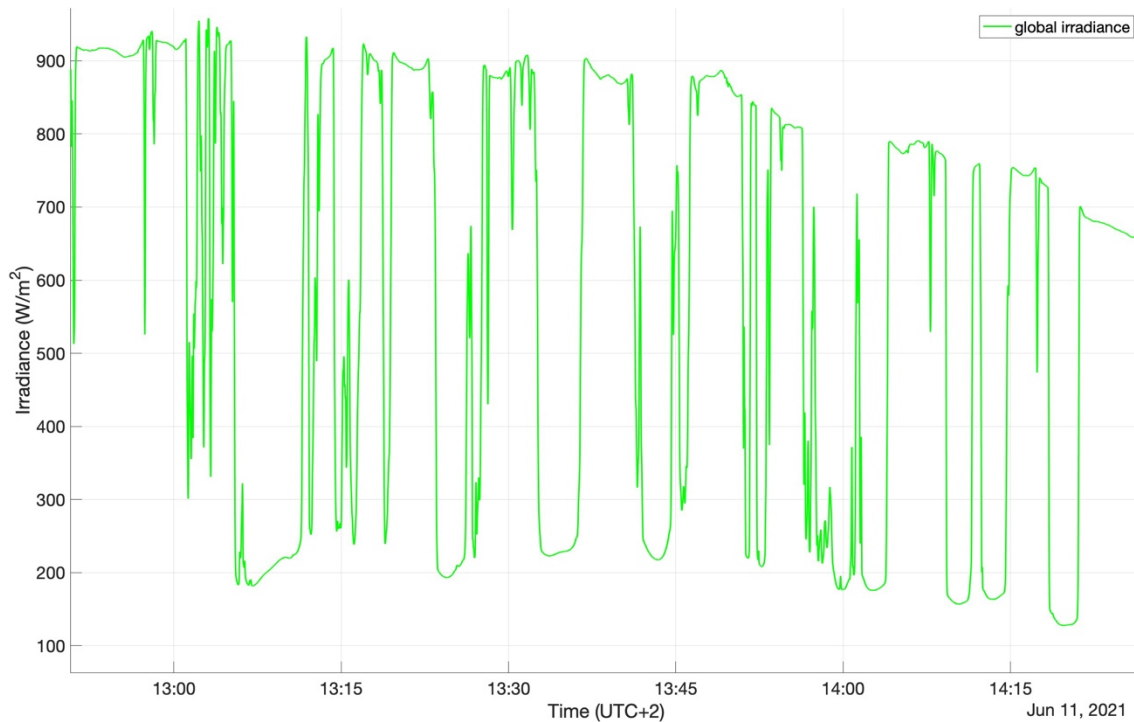


Figure 2.9. Measured global irradiance with fast-moving clouds on June 11, 2021.

Figure 2.9 illustrates significant fluctuations in global irradiance throughout the day. The cloud enhancement phenomenon amplifies the peaks of global irradiance, resulting in more rapid fluctuations [26].

The size of a PV power plant significantly influences power fluctuations, with larger plants experiencing smaller and more gradual fluctuations. In larger plants, clouds do not immediately cover all PV modules, allowing some modules to continue generating power while others are affected by cloud cover [3]. To achieve higher voltage, single PV cells are connected in series, as the voltage of a single cell is typically low. In STC, the open-circuit voltage for a crystalline silicon PV cell is approximately 0.6 V. These series-connected cells form PV modules, which are often further connected in series to create strings within the entire PV power system. The arrangement of these strings, whether in series or parallel, depends on the desired voltage and power level for the PV system [18].

3 ENERGY STORAGE SYSTEMS

The fundamental principles of ESSs, their use, and several kinds of energy storage (ES) are covered in this chapter. To mitigate the unpredictable and intermittent nature of renewable energy sources, such as PV power plants, ES devices are essential. The introduction of renewable energy sources has grown more common as the world moves toward a more sustainable and low-carbon energy future [27]. However, grid stability and reliability are challenged by the inherent variability in solar power generation caused by variables like weather and variations in solar irradiance. The additional required reserve power in PV plants aids in allowing RR limitations. In practice, this can be accomplished by operating the photovoltaic (PV) plant at less than its rated capacity. This involves disconnecting a portion of the PV arrays, effectively reducing the amount of power being supplied to the grid [28].

An alternative approach involves limiting the MPP by adjusting the conventional maximum power point tracker (MPPT) algorithms [29], [30]. The next solution is the use of an ESS [31], which can absorb or inject power to offset any violations of RR limits. Systems for storing energy are essential to mitigating these fluctuations and ensuring an uninterrupted and reliable source of electricity [32], [33]. It is logical to infer that integrating an ESS would profoundly impact the energy and economic equilibrium of the PV system and prove indispensable for the sustainability of PV systems in the future, particularly considering their high cost and short lifespan. Hence, considerations such as energy capacity, losses, and the cyclic degradation of the ESS become particularly vital. Any decrease in the amount of ESS capacity needed as well as the frequency of charge and discharge cycles would help to lower the installation and maintenance costs [11].

ES, in its broadest sense, refers to a range of methods and technologies that use certain equipment or devices to transform one type of energy into another. This energy is stored and released in a specific form when needed. More precisely, the term "electric energy storage" describes technologies and methods that physically or chemically store electrical energy and release it when needed. These methods are simply the most common and widely implemented approaches due to their effectiveness, efficiency, and practicality in various applications. The storage of electrical energy is the primary topic of ES in this thesis [33].

3.1 Fundamentals of energy storage and its applications.

The utilization of ES technology brings significant advantages to power systems, aiding in various aspects such as managing peak loads, integrating new energy sources into the grid, providing a backup power supply, and enhancing the quality of electrical energy. The disparity between peak and valley loads rises with urbanization and electrical

consumption, which makes operating power systems more difficult. ES has the potential to decrease transmission losses, optimize resource utilization, and provide financial benefits to power networks by charging during periods of low demand and discharging during peak periods through diverse types of power plants [33], [34], [35] as shown in Figure 3.1.

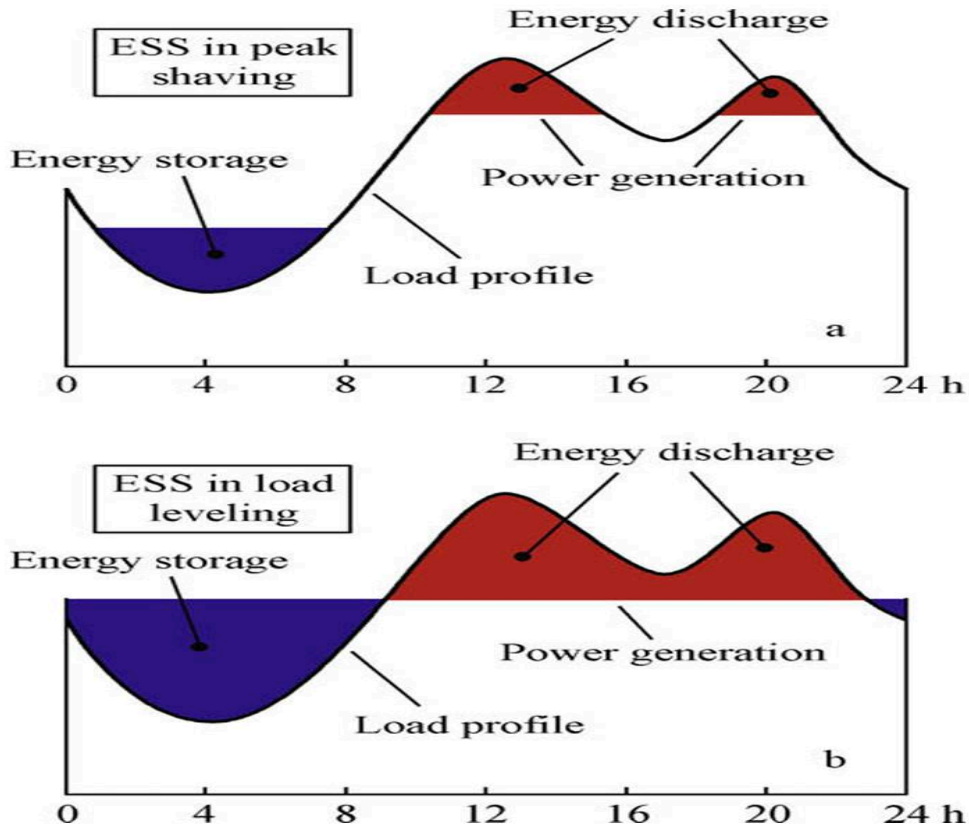


Figure 3.1. Load leveling and peak shaving using an ESS technology [36].

Power-type ES technology can be used with sensitive power loads that are prone to momentary problems with electric quality. Fast power conversion is provided by facilities with flywheels, supercapacitors, and superconductors. This lowers harmonic distortion, voltage fluctuations, and flickering. This enhances the quality of the power supply, which is particularly critical for users vulnerable to transient voltage variations [33]. Energy arbitrage involves the battery energy storage system (BESS) owner benefiting from market opportunities. Specifically, the BESS is charged and discharged during economically favorable conditions [37].

To ensure the frequency and voltage stability of the power grid, it is essential to maintain a balanced equilibrium between electricity generation and consumption. Any disparity between the two has the potential to induce significant fluctuations in the voltage level of the grid, leading to potential system issues [38]. As was noted in Chapter 2, PV power plants can have rapid fluctuations in their output powers. There is a notable possibility

that the power generated and the power consumed within the grid will differ due to the unpredictable output power from these sources. Growing amounts of renewable energy resources are likely to make it harder to keep the system stable [39], [40].

A substantial amount of the generated power from PV power plants needs to be limited when the fluctuations exceed the threshold limit. Curtailment becomes necessary primarily under two circumstances: either when the generated power is surplus to requirements, or when power production reaches the threshold limit of the grid. With the integration of an ESS, excess electrical energy can be stored and utilized during periods of rapid ramp-ups and ramp-downs [33].

Figure 3.2 demonstrates the utilization of an ESS to regulate the varying production power of a PV power plant, ensuring it stays within the defined threshold limit.

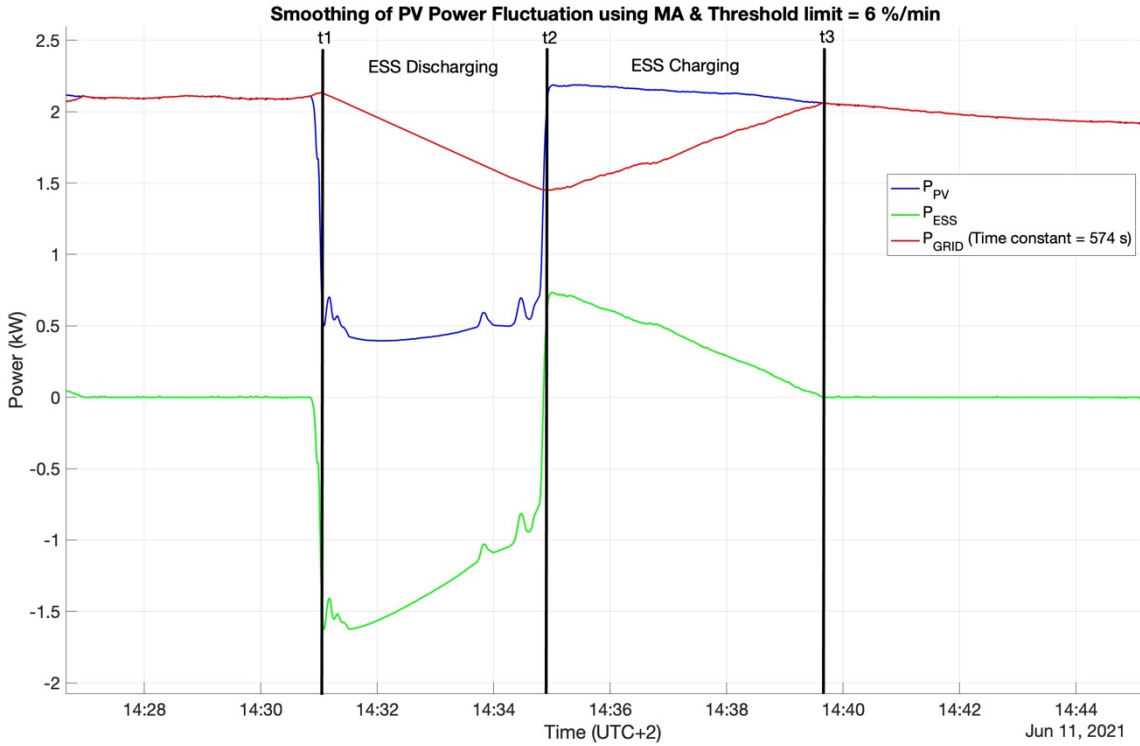


Figure 3.2. Employing an ESS to smooth out power fluctuations in a 3.23 kW PV Power plant.

In Figure 3.2, it is seen that in just a short period, the power output of the PV power plant fluctuates rapidly. The P_{grid} remains within the threshold limit, thanks to the ESS charging or discharging energy as necessary. The energy quantity, E_{ESS} , that is charged or discharged through the ESS can be expressed as

$$E_{ESS} = \int_{t_1}^{t_2} P_{ESS}(t)dt, \quad 3.1$$

where t_1 and t_2 represent the beginning and end times of the discharging period for ESS, respectively [35]. Between t_1 and t_2 , the ESS discharges power to the grid in the scenario

shown in Figure 3.2, responding to a sudden decrease in P_{PV} , preventing the P_{grid} from exceeding the threshold limit by losing a certain amount of energy. Subsequently, between t_2 and t_3 , the ESS is charging, responding to a sudden increase in P_{PV} , resulting in an energy gain for the ESS during this period.

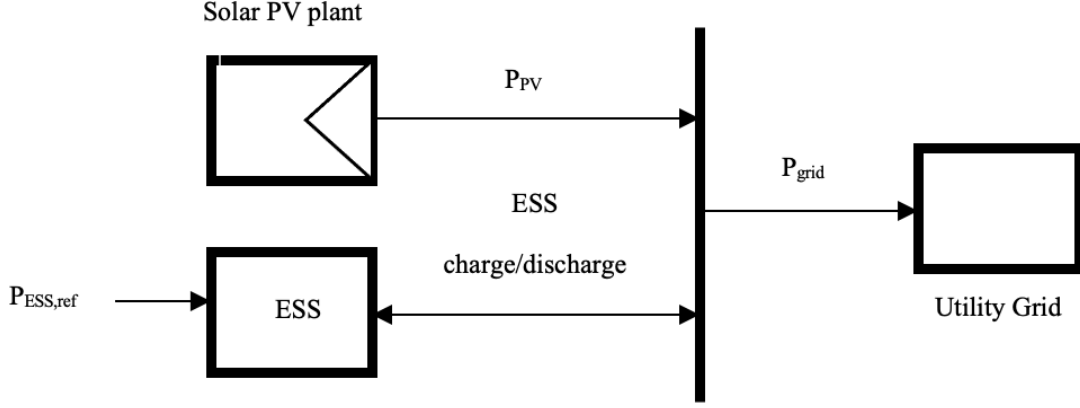


Figure 3.3. Integration of an ESS with a PV power plant to supply controlled power into the grid [16].

In Figure 3.3, the power fed into the grid (P_{grid}) and the power of the ESS (P_{ESS}) are determined by the equation

$$P_{PV} = P_{grid} + P_{ESS}, \quad 3.2$$

where, P_{PV} is the generated power of the PV power plant. The sign of P_{ESS} depends on whether the ESS is in a charging or discharging state. In this scenario, P_{ESS} is positive when the ESS is charging, indicating that it is absorbing power produced by the PV plant. Conversely, P_{ESS} is negative during discharging, indicating that the grid is receiving electricity from the ESS.

3.2 Various energy storage technologies with their characteristics

ESS technologies have been categorized in several suggested ways. These methods include classification based on response time, capacity, discharge time, efficiency, response time, and storage duration [36], [41], [42]. The prevalent method for classifying the ESS technologies is based on the energy stored [43], [44]. This classification encompasses mechanical, electrochemical, electrical, chemical, thermo-chemical, and thermal storage methods [45] as shown in Figure 3.4.

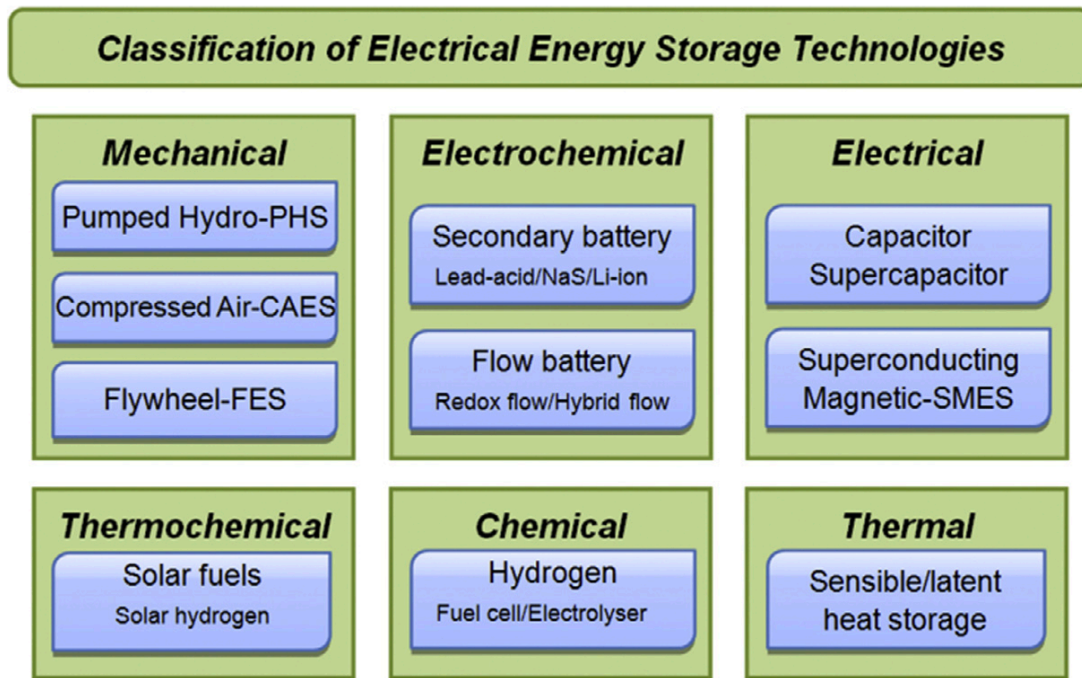


Figure 3.4. Categorization of ESS technologies based on the form of energy stored [45].

The upcoming subchapters offer a detailed introduction and explanation of each ESS technology type, covering aspects such as power rating, cycle efficiency, and lifespan. Additionally, specific energy and specific power are crucial parameters in assessing ES solutions. Specific energy denotes the maximum energy capacity per unit weight, while specific power is determined by dividing the maximum output power of the unit by its weight [35].

3.2.1 Pumped Hydroelectric Storage

Pumped hydroelectric storage (PHS) is characterized by its technical advancement, substantial capacity, and extensive operational history. As of 2012, PHS holds the dominant share of bulk storage capacity worldwide, with an installed capacity ranging from 127 to 129 GW, constituting over 99 % of the total. PHS systems contribute approximately 3 % to global electricity generation [42], [46]. In a distinctive PHS facility, there exist two water reservoirs situated in the upper and lower regions. During off-peak periods, water is pumped from the lower reservoir to the upper reservoir, while during peak hours, it is released back into the lower reservoir. The water from the upper reservoir drives the water turbines, generating electricity through the connected generator. The stored energy is determined by the height difference between the upper and lower reservoirs, as well as the volume of retained water. The rated power of PHS plants is determined by factors such as water pressure, flow rate, and the rated power of the generator and turbine [30].

The power capacity of PHS plants ranges from 1 MW to 3003 MW, with cycle efficiencies typically falling between 70 % and 85 %, and a projected lifespan exceeding 40 years [36], [47]. PHS plants are employed for tasks including frequency regulation, time-shifting, and providing reserve power. While effective, these plants encounter challenges such as limitations in site selection, extended construction durations, and substantial capital investments [45].

3.2.2 Compressed air energy storage

One unit of compressed air energy storage (CAES) can provide more than 100 MW of output electricity. Excess electricity is utilized during periods of low demand to operate a reversible motor/generator unit, which then drives a series of compressors responsible for propelling air into a storage container. This energy-storing device, which stores energy as high-pressure air, can be either an above-ground tank or an underground cavern. A heat source is used to heat the compressed air that has been stored in case there is not enough generation power to meet the load demand. The sources of heat include the combustion of fossil fuels or the heat extracted during compression. Turbines serve as the ultimate components that harness the energy from compressed air, while a recuperator unit recycles the waste heat from the exhaust.

The CAES system can be configured to accommodate a range of capacities, spanning from small to large scales. This technology provides moderate response times and effective performance at partial loads. Grid-related applications, such as frequency and voltage regulation, peak shaving, and load shifting, utilize large-scale CAES plants. The CAES exhibits interoperability with renewable energy sources by offering an output power smoothing mechanism. Choosing suitable locations for large-scale CAES facilities is a key challenge during implementation, as it significantly influences the initial investment cost of the plant. Moreover, CAES technology exhibits a comparative disadvantage in round-trip efficiency compared to alternatives like PHS and battery storage [45]. CAES facilities are available in a range of power capacities, spanning from 100 MW to 1 GW, with round-trip efficiencies typically falling between 40 % and 70 %, and a projected lifespan of 20 to 40 years. CAES has a low round-trip efficiency and needs high capital investments [48], [49].

3.2.3 Flywheel energy storage

The flywheel energy storage (FES) system comprises five fundamental components: the flywheel, reversible electric motor or generator, vacuum enclosure, power electronics unit, and a set of bearings [50]. The flywheel system uses electricity to accelerate or decelerate the flywheel and integrates with a motor or generator. To minimize energy loss from air resistance and wind shear, the FES system can be situated within a high vacuum

environment. The amount of energy stored is determined by the inertia of the flywheel and its rotational speed. There are two variants of FES: low-speed and high-speed. Low-speed FES is suitable for medium to high power and short-term applications. High-speed FES systems often employ non-contact magnetic bearings to reduce wear and enhance performance. High-speed FES is increasingly being utilized in applications such as aerospace and traction industries for superior power quality and ride-through power services [51].

High-speed composite rotors have the potential to achieve a specific energy of up to 100 Wh/kg, whereas low-speed flywheels offer a specific energy of only 5 Wh/kg. High-speed composite flywheel systems often entail significantly higher costs compared to conventional metal flywheel systems. Beneficial aspects of FES include relatively high power density, absence of depth-of-discharge effects, excellent cycle efficiency (up to 95 % at rated power), and straightforward maintenance requirements [50], [51], [52].

Despite their limited capacity, FES devices typically possess the capability to deliver high power outputs for short durations. Consequently, unless integrated with other ESS or power generation systems such as batteries or fuel-fired generators, they are not commonly employed as standalone backup power sources. A primary drawback of FES is the power loss experienced by flywheel devices during idle or standby periods. Consequently, self-discharge rates can be relatively substantial, reaching up to 20 % of the stored capacity per hour.

3.2.4 Battery energy storage

Rechargeable batteries are among the most commonly utilized battery energy storage (BES) technologies, extensively employed in both industrial and everyday settings. In BES, numerous electrochemical cells are linked together either in series or parallel configurations to generate electricity at the desired voltage. Each cell comprises an electrolyte, which may be solid, liquid, or viscous, along with two electrodes: a cathode and an anode [64, 65]. Energy can be converted bidirectionally by a cell from electrical to chemical forms. During discharge, electrochemical reactions occur simultaneously at both the anodes and cathodes. Electrons are transferred from the anodes to the external circuit, where they are subsequently collected at the cathodes. Conversely, during charging, reverse reactions take place, and an external voltage is applied to the two electrodes to replenish the battery. Many applications, such as medical, aerospace, electric grid support, marine, and transportation systems, and so on, use batteries extensively [30].

Various types of BES systems are available in the market, including lead-acid, lithium-ion (Li-ion), sodium-sulfur (NaS), nickel-cadmium (NiCd) batteries, and others.

However, this subchapter primarily focuses on lead-acid and Li-ion batteries due to their predominant usage in the market. Lead-acid batteries are the most commonly utilized rechargeable batteries. They consist of a cathode composed of PbO_2 , an anode made of Pb , and sulfuric acid serving as the electrolyte. Lead-acid batteries are characterized by fast response times, low daily self-discharge rates (below 0.3 %), reasonably high cycle efficiencies (ranging from 63 % to 90 %), and cost-effectiveness with relatively low capital expenditures. However, utility-scale installations of lead-acid batteries remain limited globally, primarily due to their relatively short cycling durations (up to 2000 cycles), lower energy density (ranging from 50 to 90 Wh/L), and specific energy (ranging from 25 to 50 Wh/kg) [36].

In a Li-ion battery, the anode consists of graphitic carbon, while the cathode is typically composed of lithium metal oxides such as LiCoO_2 and LiMO_2 . Typically, the electrolyte comprises a non-aqueous organic liquid containing dissolved lithium salts, such as LiClO_4 [53]. Li-ion batteries are considered suitable for applications where rapid response time, compact size, and/or lightweight equipment are critical. They offer millisecond-level response times and exhibit energy densities ranging from 1500 to 10,000 W/L, specific energies between 75 and 200 Wh/kg, and specific powers from 150 to 2000 W/kg. Li-ion batteries can achieve cycle efficiencies of up to 97 %. However, one of their key drawbacks is the impact of cycle depth of discharge on their lifespan. Additionally, Li-ion battery packs often require an onboard computer to regulate their operation, leading to increased overall costs [36], [42], [52].

3.2.5 Supercapacitor

Supercapacitors consist of two conductive electrodes, an electrolyte, and a porous membrane separator, and they are alternatively known as electric double-layer capacitors or ultracapacitors [53]. Supercapacitors share structural traits with both electrochemical batteries and conventional capacitors. Static charge is the result of energy being stored on the surfaces between the two conducting electrodes and the electrolyte. Nanomaterials are frequently used in high-performance supercapacitors to improve capacitance by expanding the electrode surface area. The power and energy densities of supercapacitors fall between those of traditional capacitors and rechargeable batteries.

Supercapacitors are renowned for their extended cycling lifetimes, exceeding 50,000 cycles, and exhibit high cycle efficiencies ranging from 84 % to 97 %. Their charge and discharge times, at their rated power, typically span from 1 to 30 seconds, boasting remarkably high specific power and energy density levels of 2000 to 5000 W/kg and 20,000 to 30,000 Wh/m³, respectively. However, their specific energy and energy density remain relatively modest, ranging from 2 to 5 Wh/kg and 10,000 Wh/m³, respectively, primarily due to challenges associated with ion access to the porous

electrode surface [54]. Supercapacitors exhibit a notable daily self-discharge rate ranging from 5 % to 40 % and are associated with high capital costs. Consequently, they are well-suited for applications necessitating short-term storage but may not be optimal for extensive, long-term storage purposes [36], [53].

3.2.6 Superconducting magnetic energy storage

A standard setup for a superconducting magnetic energy storage (SMES) system consists of three primary components: a unit containing a superconducting coil, a subsystem for power conditioning, and a subsystem for refrigeration and maintaining vacuum conditions [53], [55]. The SMES system functions by storing electrical energy within the magnetic field generated by the DC passing through the superconducting coil, which has been cooled cryogenically below its critical superconducting temperature. Typically, when electric current passes through a coil, energy is dissipated as heat due to wire resistance. However, if the coil is constructed from a superconducting material such as mercury or vanadium and is in its superconducting state (usually achieved at extremely low temperatures), it exhibits zero resistance, enabling efficient storage of electrical energy with minimal losses. One commonly utilized superconducting material is Niobium-Titanium, which possesses a critical superconducting temperature of 9.2 K [36]. During discharge, the SMES system can release the stored electrical energy back into the alternating current system through a connected power converter module. The amount of energy stored is determined by factors such as the self-inductance of the coil and the electric current flowing through it [56].

Commercially, SMES devices ranging from 0.1 to 10 MW have been deployed. Key attributes of SMES include a relatively high power density (up to 4000 W/L), rapid response times at the millisecond level, exceptionally fast full discharge times (less than 1 minute), high cycle efficiency (ranging from 95 % to 98 %), and an extended lifespan of up to 30 years. Unlike rechargeable batteries, SMES devices can discharge nearly all stored energy with minimal degradation even after numerous full cycles. However, they are associated with drawbacks such as high initial capital costs and a significant daily self-discharge rate (10–15 %) [36]. Furthermore, the coil is susceptible to minor temperature fluctuations, leading to potential energy losses. Based on the information provided, SMES is well-suited for short-term storage applications within power and energy systems and is anticipated to contribute significantly to the expanded utilization of intermittent renewable energy sources [55].

3.2.7 Hydrogen storage and fuel cell

Systems that store energy using hydrogen use two different methods to generate power and store energy. The standard procedure is to create hydrogen using a water electrolysis

device. Hydrogen can then be piped or stored for later use in high-pressure containers [53]. The regenerative fuel cell is a crucial piece of technology when using stored hydrogen to generate energy. Fuel cells can release electrical and thermal energy while converting the chemical energy found in hydrogen and oxygen into electricity. The overall reaction is: $2H_2 + O_2 \rightarrow 2H_2O + \text{energy}$.

There are six primary classifications of fuel cells, which are determined by the chosen fuel and electrolyte: These include alkaline fuel cells (AFC), phosphoric acid fuel cells (PAFC), solid oxide fuel cells (SOFC), molten carbonate fuel cells (MCFC), proton exchange membrane fuel cells (PEMFC), and direct methanol fuel cells (DMFC) [57]. Hydrogen ESSs are offered with power capacities ranging from 1 MW to 50 MW, exhibiting round-trip efficiencies of approximately 25 % to 50 %, and boasting lifespans spanning from 5 to 30 years [35], [36].

3.2.8 Solar fuels

Solar fuel technology represents a novel approach to ESS, encompassing various methods to produce fuels using solar energy. These methods include natural photosynthesis, artificial photosynthesis, and thermochemical approaches. Solar energy is harnessed to convert water and/or carbon dioxide into oxygen and other materials, storing the energy in chemical bonds. Artificial photosynthesis relies on catalysts like Ruthenium (Ru), Palladium (Pd), and Rhenium (Re) to capture sunlight and facilitate electron movement for water-splitting [36], [58].

In contrast, the thermochemical approach utilizes thermal processes to produce solar fuels, requiring high temperatures generated in a closed environment to split water. This method is more reliant on intense sunlight compared to other approaches. Concentrated solar radiant energy is used in conjunction with heliostats to initiate an endothermic chemical transformation in a reaction vessel, resulting in the production of hydrogen, carbon monoxide, and other materials [59], [60].

Currently, solar fuel technology is in the developmental stage, with potential power ratings of up to 20 MW and specific energy estimates ranging from 800 Wh/kg to 100,000 Wh/kg. Storage duration can vary from a few hours to several months. However, there are some drawbacks, such as the dependence of water-splitting catalysts on scarce and expensive elements in artificial photosynthesis. Additionally, solar fuel facilities require large areas to accommodate devices for concentrating sunlight, particularly when utilizing the thermochemical approach [36], [58], [59].

3.2.9 Thermal energy storage

Thermal Energy Storage (TES) covers a range of technologies designed to store available heat energy using different approaches within insulated storage. A typical TES system comprises a storage medium housed in a reservoir or tank, along with ancillary components such as a packaged chiller or built-up refrigeration system, piping, pumps, and control systems. TES systems can be categorized based on their operating temperature into two main groups: low-temperature TES and high-temperature TES.

The low-temperature TES includes aquiferous low-temperature TES and cryogenic energy storage. Aquiferous low-temperature TES systems typically involve processes such as water cooling or icing and reheating, making them suitable for applications like peak shaving and industrial cooling loads [36], [61]. Cryogenic energy storage, on the other hand, utilizes cryogenics like liquid nitrogen or liquid air for electrical and thermal energy conversion. An example of this is Liquid Air Energy Storage (LAES), which is gaining attention due to its high expansion ratio and power densities compared to gaseous air.

High-temperature TES includes latent heat TES, sensible heat TES, and concrete thermal storage. Latent heat TES employs Phase Change Materials (PCMs) as storage media, utilizing the energy absorption or emission during the liquid-solid transition of these materials at a constant temperature. Concrete thermal storage, on the other hand, utilizes concrete or castable ceramics to store heat energy, often with synthetic oil as a heat transfer fluid.

Each of these TES technologies has unique features and applications. For example, latent heat storage offers relatively high storage density with small reservoir dimensions, making it suitable for building applications [62]. Cryogenic energy storage is anticipated to play a role in future grid power management due to its potential for high power densities. The choice of TES technology depends on factors such as the desired storage capacity, operating temperature range, and specific application requirements.

TES systems offer several advantages, including the ability to store large quantities of energy safely, minimal daily self-discharge losses (typically ranging from 0.05 % to 1 %), and a reservoir with favorable energy density and specific energy (ranging from 80 to 500 Wh/L and 80 to 250 Wh/kg, respectively). Moreover, TES systems are economically viable, however, it is worth noting that TES systems typically exhibit low cycle efficiencies, typically ranging from 30 % to 60 % [36], [61], [63].

Despite this limitation, TES has found widespread use across various applications, including load shifting and electricity generation for heat engine cycles. These systems play a crucial role in enhancing energy efficiency and grid stability while also facilitating the integration of renewable energy sources into the power grid [61].

3.3 Integration of ESSs with PV power plants

Fluctuations in solar irradiance throughout the day and across seasons result in fluctuations in the voltage and frequency of the power system, affecting its stability and quality. Consequently, to reduce disturbances, ESSs with a long-life cycle and fast response are employed. Because the output of the PV power plants fluctuates quickly, it is essential to integrate ESSs with high charge and discharge powers and quick response times. Additionally, the connected ESS should be able to withstand several cycles, particularly in situations where there is a quick change in cloud cover and the PV power plant has repeated power ramps [64]. Employing a hybrid ESS could offer advantages for photovoltaic power plants. A long-term energy storage solution would supply power during nighttime periods when the PV plant is inactive, while a short-term energy storage system would mitigate sudden fluctuations. Furthermore, using a supercapacitor instead of a battery for short-term stabilization in a hybrid ESS may increase the total lifespan of the ESS [64], [65].

As the size of a power plant increases, the fluctuations in output power decrease, consequently reducing the necessary relative power and energy capacity for an ESS. Numerous studies have explored the integration of ESS with PV power plants, revealing a relationship between the sizing needs of the ESS and the scale of the power plant [12], [13], [66]. However, in this thesis, the same rated PV power is used for the sizing of the ESS focused on the comparison between two different strategies, i.e., MA and LPF. Ultimately, comparing the size of the ESS between them with and without the threshold limits and using different time constants.

3.4 Control strategies and their impact on ESS sizing

Diverse strategies and algorithms are employed to manage output power fluctuations, ensuring a smoother power output to the grid, which in turn acts as a reference power for an ESS. Three general categories can be used to organize these controlling strategies: filter-based strategies, RR-based algorithms, and MA and exponential smoothing (EXS)-based strategies [16]. In an optimal scenario with an ideal converter and battery, the energy stored in the ESS should remain consistent at the beginning and end of each day, as per the mean value principle. As a result, there is no requirement for any state-of-charge (SOC) control technique to halt the continuous discharge of the battery [11].

The reference power in the MA and EXS strategies is determined by averaging the PV output power across a given period or several data points. While these strategies are straightforward and computationally efficient, they increase the required capacity for the ESS and force continuous ESS operation, leading to a reduced lifetime [16]. The smoothed power supplied to the grid in the MA strategy is defined by Equation 3.3.

$$P_{\text{grid,MA}}(i) = \frac{\sum_{j=i-\tau_{\text{MA}}+1}^i P_{\text{PV}}(j:i)}{\tau_{\text{MA}}}, \quad 3.3$$

where, τ_{MA} is the time window (time constant); the higher the value of τ_{MA} , the higher the smoothing of the fluctuations [67].

Filter-based techniques, such as particle, Kalman, high-pass, and low-pass filters, permit intended frequency signals to go through while attenuating unwanted ones. Their benefits and drawbacks are similar to those of MA and EXS smoothing techniques, but they typically require less ESS capacity [16]. In the first-order LPF strategy, the smoothed power feed into the grid is given by Equation 3.4.

$$P_{\text{grid,LPF}}(i) = \frac{P_{\text{PV}}(i)}{\tau_{\text{LPF}}+1}, \quad 3.4$$

where, τ_{LPF} is the filter time constant [67].

The RR of the output power of the power plant is compared to a predetermined threshold limit that is permitted in the grid using MA and LPF algorithms. Smoothing is not required if the RR between the consecutive output powers does not exceed the threshold limit. By implementing the threshold limit, over-smoothing can be avoided for those periods where the RR of the PV output power is already within the threshold limit. Therefore, the size of the ESS can be reduced, and the lifetime of the ESS can be extended. Also, these strategies require less computational work [16].

The size of the ESS is determined by various criteria, including the type of power system, its size, and its intended use. The size of the required ESS is determined by the control technique that is chosen [14], [16]. The necessary maximum power and energy capacity are basic size parameters. Different methodologies can be used to determine these parameters; some take into account the maximum values that have been seen in experiments [12], [14]. Various sizing methods balance technical and techno-economic perspectives, often emphasizing cost reduction [68]. However, many sizing algorithms are complex, considering economic feasibility alongside technical requirements [69], [70]. This thesis focuses solely on technical parameters and considers the idealities of the system when sizing the ESS using the MA and LPF strategies.

4 MEASUREMENTS AND MODELING

This chapter provides an overview of the measurement data and methodologies employed in conducting the simulations. All data utilized in this study originates from measurements conducted at the Finnish Solar PV Power Station Research Plant situated at Tampere University. This research facility, positioned atop a university building, collected data on various parameters such as ambient temperature, PV module back-side temperature, global irradiance, and PV output power. The study plant is composed of 69 NP190GKg PV modules, which have a 13.1 kW_p peak power overall. Each PV module possesses a P_{MPP} of 190 W, and the configuration was arranged to enable an $I-V$ sweep from a string comprising 17 modules, totaling a combined peak power of 3.23 kW. The measurements of PV output power and time stamp will be utilized for the simulation. The information gathered on the day of the measurement was kept in a cloud service for later review or download to a PC for simulation purposes. Since the emphasis of this thesis is on mitigating rapid power fluctuations in a PV power plant, it was imperative to capture even the most rapid irradiance changes. It was observed that a sampling frequency of 10 Hz sufficed to detect even the quickest fluctuations. However, a sampling frequency of 1 Hz was employed for the measurements of the $I-V$ curves [71].

4.1 Measurements

The pyranometer CMP22 measured the global solar irradiance received on the horizontal plane; the pyranometer CMP21 measured the diffuse solar irradiance on the horizontal plane; and the SPLite2 photodiode sensor, identified as S19, measured the global solar irradiance received on the module plane while maintaining the same 45° tilt angle as the module located on the rooftop of the building. Concurrently, a Pt100 temperature sensor, which was similarly built into the same PV module as the photodiode sensor, was used to monitor the temperature on the backside of the module. The measurements were carried out on the 11th and 15th of June, 2021 [71].

4.2 Modeling of energy storage systems

ESS sizing computations consider the RR in the output power (P_{PV}) of PV power plants that surpasses the threshold limit. These threshold limits also expressed as the percentage of the rated capacity over a time interval in minutes, play a crucial role. In this thesis, a common RR limit of 10 %/min is utilized, as often seen in relevant research studies. Consequently, the applied RR limit in this thesis remains at 10 %/min. Various threshold limits, namely 2 %/min, 4 %/min, 6 %/min, 8 %/min, and 10 %/min, are examined, corresponding to 20 %, 40 %, 60 %, 80 %, and 100 % of the RR limit, respectively.

The MA and LPF control algorithms are the ones implemented for the ESS. The MA and LPF control algorithms applied in ref. [67] are comparable to the MA and LPF control strategies utilized in this thesis. The objective of the algorithm is to reduce the required energy capacity of the ESS by activating it solely when the threshold limit is exceeded. In addition to operating the ESS, the control algorithms calculate the required size of the ESS.

The maximum power of a PV plant that can fluctuate in a second with a threshold limit of 2 %/min is determined by

$$P_{\text{threshold_limit}} = \frac{0.02 * P_{\text{nom}}}{60 \text{ s}}, \quad 4.1$$

where, P_{nom} is the nominal power of the PV plant. For the first iteration in MATLAB, the first values of P_{grid} and P_{ESS} are $P_{\text{PV}}(1)$ and 0, respectively.

The P_{grid} for the next iteration using the MA strategy is calculated as

$$P_{\text{grid}}(t) = \frac{\text{sum}(P_{\text{PV}}(\max(1, t - \tau_{\text{MA}} + 1):1))}{\tau_{\text{MA}}}, \quad 4.2$$

The P_{grid} for the next iteration using the LPF strategy is calculated as

$$P_{\text{grid}}(t) = \alpha * P_{\text{PV}}(t) + (1 - \alpha) * P_{\text{grid}}(t - 1), \quad 4.3$$

where, $\alpha = 1/(1 + \tau_{\text{LPF}})$

The power and energy of the ESS for the next iteration are calculated as,

$$P_{\text{ESS}}(t) = P_{\text{PV}}(t) - P_{\text{grid}}(t), \quad 4.4$$

and

$$E_{\text{ESS}}(t) = E_{\text{ESS}}(t - 1) + P_{\text{ESS}}(t) * T_s, \quad 4.5$$

since the sampling frequency was 1 Hz, therefore, the value of T_s is 1 s. The MATLAB code to smooth the PV output power and compute the size of the ESS for the MA based control algorithm is shown in Appendix 1.

To determine the sizing of the ESSs without the threshold limit, the control algorithms of MA and LPF continuously adjust the grid power as required. However, a challenge arises with these novel control strategies while implementing the threshold limits. Even after incorporating the threshold limit in the PV output power, the power RRs in the power supplied to the grid may still exceed the threshold limit at times when the control strategy algorithm is toggled on or off. This occurs because, in certain situations, when the algorithm is activated or deactivated, there can be a significant disparity between the actual

PV power output and the power calculated by the algorithm. For example, during a rapid increase in generated PV power, such as when a shadow moves away, the actual power output remains high while the calculated power from the algorithm is notably low.

To solve this issue, first, the power fed to the grid is determined depending on whether the RR in the PV power is above or below the threshold limit. After that, the current calculated grid power is deducted from the previous grid power to find the RR and compare it with the threshold limit. If the RR is above or equal to the threshold limit, then the current grid power is recalculated by ramping up or down the previous grid power to a new value where the RR in the current grid power is near the threshold limit. In this thesis, 99 % of the threshold limit is allowed in the previous grid power.

5 RESULTS AND DISCUSSION

This chapter is about the simulation results of the sizing of the ESSs by using different smoothing strategies, time constants, and threshold limits. Subchapter 5.1 explains the sizing of the ESSs with two different smoothing strategies. Subchapter 5.2 explains the sizing of the ESSs with different threshold limits and without threshold limits. Subchapter 5.3 explains the size of the ESSs with three different time constants. The results are demonstrated by using the measurements carried out on the 11th and 15th of June, 2021. The results of the ESS sizing are compared with the previous works of literature. Subchapter 5.4 discusses the findings and implications.

5.1 Sizing of the ESSs with two different smoothing strategies without using the threshold limit

This subchapter introduces the difference in the power and energy capacities of the ESSs between MA and LPF strategies. Tables 5.1 and 5.2 present the results of the sizing of the ESS for days 11.06.2021 and 15.06.2021, respectively. The sizing quantities like energy capacity, charging and discharging power capacity, relative energy and power capacity, energy charged and discharged, energy fed to the grid, and share of energy cycled through the ESS, including the used time constants and the highest observed RR of the grid power, are shown in Tables 5.1 and 5.2. The time constants are chosen in such a way that the highest RR in the grid power without a threshold limit is observed just below the RR limit (10 %/min) so that they show similarities with the results of [67].

Table 5.1. Iterated time constants, the highest observed power ramp rates, and the sizing of the ESS with the MA and LPF control strategies for 11.06.2021.

Control Strategies	MA	LPF
Threshold limit (%/min)	-	-
Time constant (s)	454	398
Highest observed RR (%/min)	9.9863	9.9899
Energy capacity (kWh)	0.1735	0.2912
Relative energy capacity (h)	0.0537	0.0902
Charging power capacity (kW)	2.1011	2.1324
Discharging power capacity (kW)	2.038	1.9725
Relative charging power capacity (%)	65.0501	66.0186
Relative discharging power capacity (%)	63.0958	61.0666
Energy charged (kWh)	1.6645	1.7135
Energy discharged (kWh)	1.6489	1.6866
Share of energy cycled through the ESS (%)	8.7089	8.9134

In Table 5.1, it is seen that the relative energy capacity of LPF is 67.97 % higher than MA. However, there is no remarkable difference in the relative charging and discharging power capacity and the utilization rate of the ESS between the MA and LPF. Figure 5.1 shows the smoothed grid and PV output power with the MA and LPF strategies for June 11, 2021, and June 15, 2021.

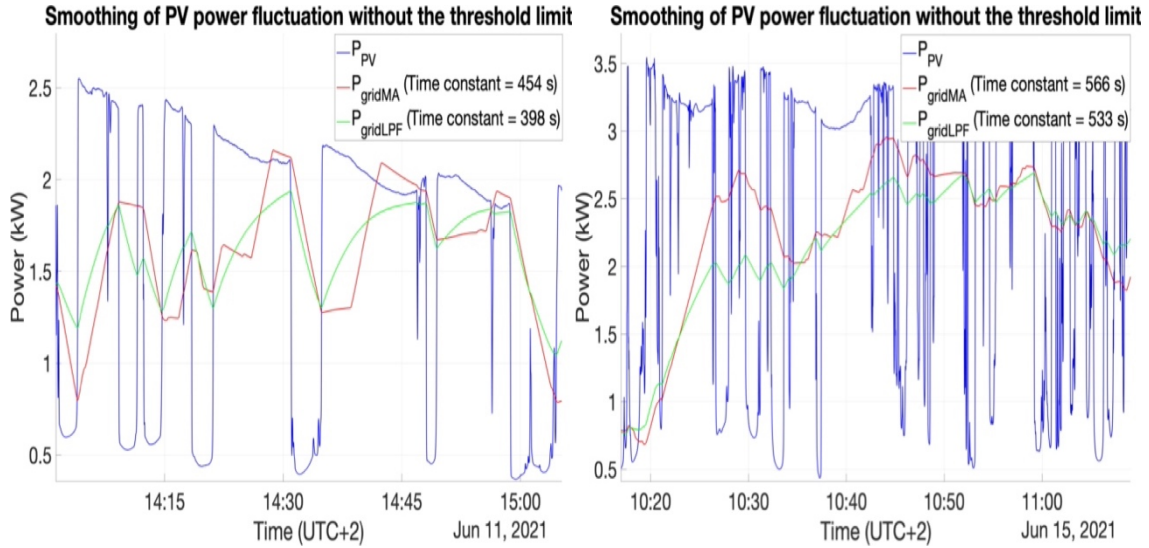


Figure 5.1. Power of the 3.23 kW PV string and smoothed grid power with MA and LPF strategies for 11.06.2021 and 15.06.2021.

In Figure 5.1, it is seen that the LPF has slightly over smoothed the PV output power compared to the MA. Therefore, it can be concluded that the utilization rate of ESSs for LPF is slightly higher than MA.

Table 5.2. Iterated time constants, the highest observed power ramp rates, and the sizing of the ESS with the MA and LPF control strategies for 15.06.2021.

Control Strategies	MA	LPF
Threshold limit (%/min)	0	0
Time constant (s)	566	533
Highest observed RR (%/min)	9.905	9.9868
Energy capacity (kWh)	0.2396	0.4395
Relative energy capacity (h)	0.0742	0.1361
Charging power capacity (kW)	2.8367	2.8656
Discharging power capacity (kW)	2.3044	2.1337
Relative charging power capacity (%)	87.8221	88.7167
Relative discharging power capacity (%)	71.345	66.0586
Energy charged (kWh)	2.535	2.573
Energy discharged (kWh)	2.528	2.5585
Share of energy cycled through the ESS (%)	16.9631	17.1766

In Table 5.2, it is seen that the relative energy capacity of LPF is 83.42 % higher than MA. However, there is no remarkable difference in the relative charging and discharging power capacity and the utilization rate of the ESS between the MA and LPF.

In general, for both Tables 5.1 and 5.2, the sizing results of the ESS between MA and LPF show similarities to ref. [67]. As the size of the PV power plant was 10 kW in ref. [67], the required relative capacities and utilization rate were higher compared to the relative capacities in Tables 5.1 and 5.2. The other reasons that affect the result are the modeled PV power data instead of measured data and also the sampling frequency; they used 10 Hz instead of 1 Hz.

5.2 Sizing of the ESSs with different threshold limits and without threshold limit

In this subchapter, the sizing of the ESSs is identified by varying the threshold limit from 2 %/min to 10 %/min by using the constant time constant and comparing these sizes of the ESSs to the ones without having the threshold limit. The time constant has been chosen in such a way that the highest RR in the grid power without a threshold limit is observed just below the RR limit (10 %/min) for compliance with the grid code. Tables 5.3 and 5.4 present the results of the sizing of the ESS for June 11, 2021, and June 15, 2021, with and without the threshold limit, respectively. The results include sizing quantities like energy capacity, charging and discharging power capacity, relative energy and power capacity, energy charged and discharged, energy fed to the grid, and the share of energy cycled through the ESS, including the used time constant and the highest observed RR of the grid power.

Table 5.3. Iterated constant time constants, the highest observed power ramp rates, and the sizing of the ESS with the MA and LPF control strategies for 11.06.2021.

Control Strategies	MA						LPF					
Threshold limit (%/min)	-	2	4	6	8	10	-	2	4	6	8	10
Time constant (s)	454						398					
Highest observed RR (%/min)	9.9863	1.9996	3.9994	5.999	7.9996	9.9994	9.9899	2	3.9994	5.9996	7.9996	9.9994
Energy capacity (kWh)	0.1735	0.5012	0.4935	0.3338	0.2542	0.2285	0.2912	0.8193	0.7002	0.4245	0.3478	0.3047
Relative energy capacity (h)	0.0537	0.1552	0.1528	0.1033	0.0787	0.0707	0.0902	0.2536	0.2168	0.1314	0.1077	0.0943
Charging power capacity (kW)	2.1011	2.0077	2.2333	2.338	2.3103	2.284	2.1324	1.9649	2.4027	2.3867	2.3708	2.3492
Discharging power capacity (kW)	2.038	2.1816	2.1197	2.079	2.0461	2.038	1.9725	2.2264	2.1409	2.127	2.1175	2.1085
Relative power capacity (%)	65.0501	67.5417	69.1419	72.3851	71.5268	70.7127	66.0186	68.9295	74.3884	73.8926	73.3988	72.7291
Energy charged (kWh)	1.6645	1.6554	1.4865	1.3908	1.2302	1.0905	1.7135	1.0041	1.0919	1.0358	0.9851	0.9485
Energy discharged (kWh)	1.6489	2.0294	1.64	1.4441	1.3492	1.2858	1.6866	2.2778	1.8036	1.5911	1.4861	1.4243
Energy fed to the grid (kWh)	18.9337	19.3232	19.1028	19.0025	19.0682	19.1445	18.9224	20.223	19.661	19.5046	19.4502	19.425
Share of energy cycled through the ESS (%)	8.7089	10.5024	8.5852	7.5993	7.0756	6.716	8.9134	11.2636	9.1735	8.1574	7.6405	7.3321

In Table 5.3, in the case of the implementation of the threshold limit for MA and LPF, the lowest required relative energy capacity at a threshold limit of 10 %/min is 54.45 % and 62.82 % lower than the highest required relative energy capacity at a threshold limit of 2 %/min, respectively. For MA, the lowest required relative power capacity at a threshold limit of 2 %/min is 6.69 % lower than the highest required relative power capacity at a threshold limit of 6 %/min. For LPF, the lowest required relative power capacity at a threshold limit of 2 %/min is only 7.34 % lower than the highest required relative power capacity at a threshold limit of 4 %/min. For MA and LPF, the lowest required utilization rate at a threshold limit of 10 %/min is 36.05 % and 34.91 % lower than the highest required relative power capacity at a threshold limit of 2 %/min respectively.

For MA and LPF, the required relative energy capacity of the ESS without the threshold limit is lower compared to all the threshold limits. The relative power capacity of the ESS without the threshold limit is lower compared to the relative power capacity of the ESS with all the threshold limits. Therefore, for MA and LPF, the required relative energy capacity of the ESS without the threshold limit is 65.4 % and 64.43 % lower than the highest required relative energy capacity at a threshold limit of 2 %/min, respectively. For MA and LPF, the relative power capacity of the ESS without the threshold limit is 10.13 % and 11.25 % lower than the highest required relative power capacity at a threshold limit of 6 %/min and 4 %/min respectively.

For MA, the utilization rate of the ESS without the threshold limit is lower compared to the threshold limits (≤ 2 %/min). However, the utilization rate of the ESS without the threshold limit is higher compared to the threshold limits (> 2 %/min). Therefore, for the threshold limits (≤ 2 %/min), the utilization rate of the ESS without the threshold limit is 17.08 % lower than the highest utilization rate at a threshold limit of 2 %/min. In contrast, for the threshold limits (> 2 %/min), the utilization rate of the ESS without the threshold limit is 32.29 % higher than the utilization rate at a threshold limit of 10 %/min. For LPF, the utilization rate of the ESS without the threshold limit is lower compared to the threshold limits (≤ 4 %/min). However, the utilization rate of the ESS without the threshold limit is higher compared to the threshold limits (> 4 %/min). Therefore, for the threshold limits (≤ 4 %/min), the utilization rate of the ESS without the threshold limit is 20.87 % lower than the highest utilization rate at a threshold limit of 2 %/min. In contrast, for the threshold limits (> 4 %/min), the utilization rate of the ESS without the threshold limit is 21.57 % higher than the lowest utilization rate at a threshold limit of 10 %/min.

Table 5.4. Iterated constant time constants, the highest observed power ramp rates, and the sizing of the ESS with the MA and LPF control strategies for 15.06.2021.

Control Strategies	MA						LPF					
Threshold limit (%/min)	-	2	4	6	8	10	-	2	4	6	8	10
Time constant (s)	566						533					
Highest observed RR (%/min)	9.905	2	3.999	5.9978	7.9978	10	9.9868	1.9998	3.9994	5.9996	7.999	10
Energy capacity (kWh)	0.2396	0.9081	0.5113	0.3831	0.3259	0.3141	0.4395	1.4125	0.7984	0.5608	0.5283	0.5032
Relative energy capacity (h)	0.0742	0.2812	0.1583	0.1186	0.1009	0.0972	0.1361	0.4373	0.2472	0.1736	0.1635	0.1558
Charging power capacity (kW)	2.8367	2.8428	2.8433	2.8498	2.837	2.8367	2.8656	2.8344	2.9612	2.9304	2.9222	2.9114
Discharging power capacity (kW)	2.3044	2.2846	2.3139	2.3079	2.3045	2.3849	2.1337	2.393	2.4107	2.447	2.6109	2.6067
Relative power capacity (%)	87.8221	88.0113	88.029	88.2279	87.8329	87.8221	88.7167	87.7528	91.6784	90.724	90.4709	90.1365
Energy charged (kWh)	2.535	2.7733	2.4885	2.3001	2.1219	1.9837	2.573	2.3301	2.1918	1.9807	1.8027	1.7126
Energy discharged (kWh)	2.528	2.7115	2.4155	2.2048	2.083	1.9895	2.5585	2.8609	2.4063	2.2854	2.2395	2.1627
Energy fed to the grid (kWh)	14.9027	14.8479	14.8368	14.8144	14.8708	14.9155	14.8952	15.4405	15.1242	15.2144	15.3465	15.3598
Share of energy cycled through the ESS (%)	16.9631	18.2619	16.2807	14.8144	14.0074	13.3385	17.1766	18.5283	15.9103	15.0215	14.5931	14.0805

In Table 5.4, in the case of the implementation of the threshold limit for MA and LPF, the lowest required relative energy capacity at a threshold limit of 10 %/min is 65.43 % and 64.37 % lower than the highest required relative energy capacity at a threshold limit of 2 %/min, respectively. For MA, the required relative power capacities are almost the same for all the threshold limits. For LPF, the lowest required relative power capacity at a threshold limit of 2 %/min is only 4.28 % lower than the highest required relative power capacity at a threshold limit of 4 %/min. For MA and LPF, the lowest required utilization rate at a threshold limit of 10 %/min is 26.96 % and 24.01 % lower than the highest required relative power capacity at a threshold limit of 2 %/min respectively.

For MA and LPF, the required relative energy capacity of the ESS without the threshold limit is lower compared to all the threshold limits. The relative power capacity of the ESS without the threshold limit is lower compared to the relative power capacity of the ESS with all the threshold limits. For MA, the relative power capacity of the ESS without the threshold limit is lower and equal compared to the relative power capacity of the ESS with the threshold limits (≤ 8 %/min and 10 %/min) respectively. Nonetheless, there is no big difference in the relative power capacity of the ESS without the threshold limit compared to the ones with the threshold limit. For LPF, the required relative power capacity of the ESS without the threshold limit is lower than the required relative power capacity of the ESS with the threshold limits (≥ 4 %/min). The relative power capacity of the ESS without the threshold limit is 3.23 % lower than the highest required relative power capacity at a threshold limit of 4 %/min.

For MA and LPF, the utilization rate of the ESS without the threshold limit is lower compared to the threshold limits (≤ 2 %/min). However, the utilization rate of the ESS without the threshold limit is higher compared to the threshold limits (> 2 %/min). Therefore, for the threshold limits (≤ 2 %/min), the utilization rate of the ESS without the threshold limit is 7.11 % and 7.3 % lower than the highest utilization rate at a threshold limit of 2 %/min, respectively. In contrast, for the threshold limits (> 2 %/min), the utilization rate of the ESS without the threshold limit is 27.17 % and 21.99 % higher than the lowest utilization rate at a threshold limit of 10 %/min, respectively.

Figures 5.2–5.5 present the maximum observed RR in the grid power, relative energy, power capacities, and utilization rates of the ESSs as a function of the applied threshold limit.

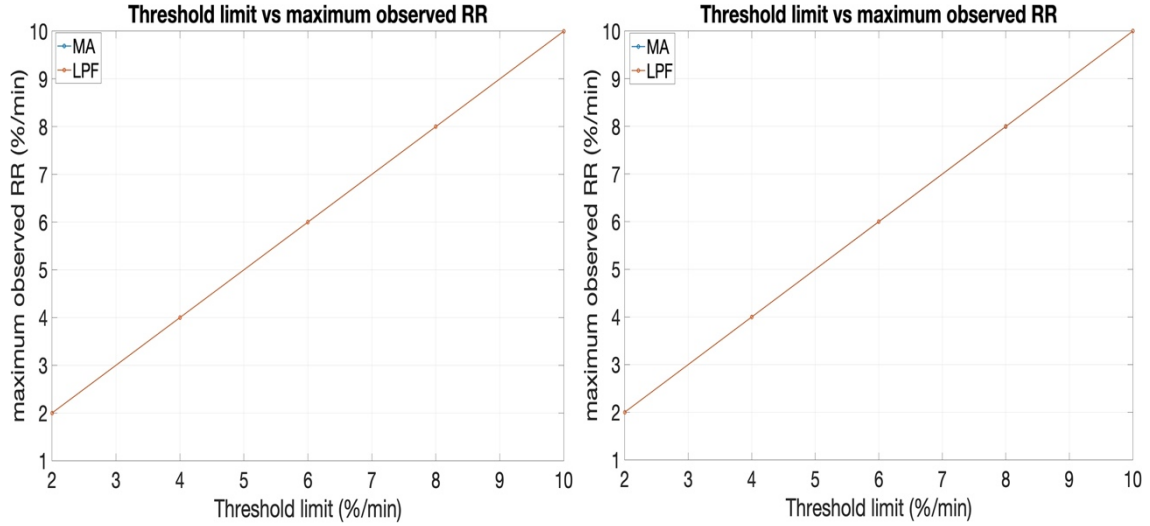


Figure 5.2. Maximum observed RR in the grid power as a function of threshold limits for 11.06.2021 (left) and 15.06.2021 (right).

Figure 5.2 illustrates that the highest observed RR in the grid power is less than or equal to the applied threshold limits for both MA and LPF strategies. Therefore, it is concluded that the algorithm allows the maximum RR until the threshold limit.

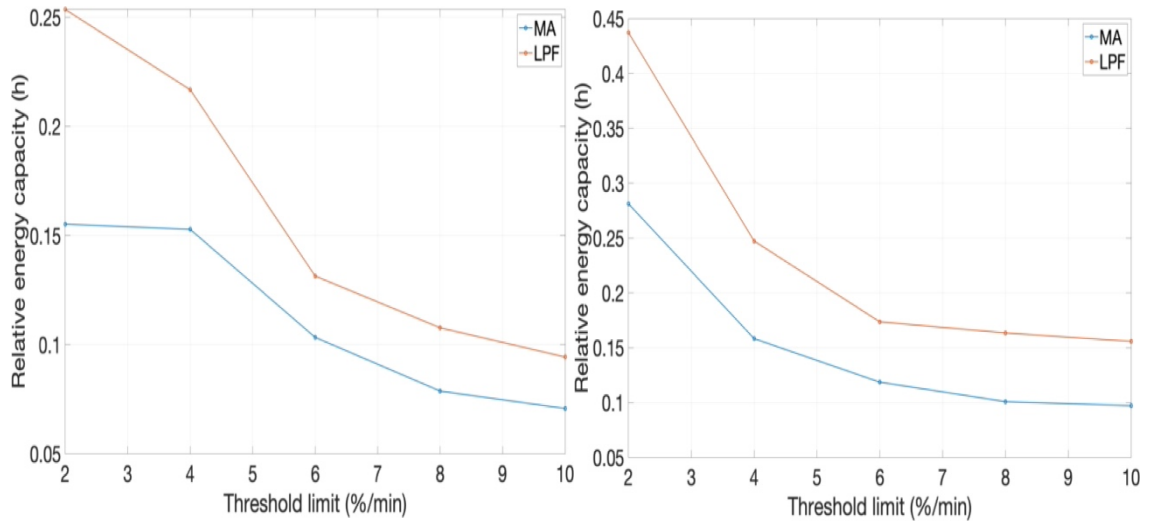


Figure 5.3. Required relative energy capacities of the ESSs as a function of threshold limits for 11.06.2021 (left) and 15.06.2021 (right).

In Figure 5.3, it is seen that an increase in the threshold limit decreases the required energy capacity of the ESS, which shows similarities with the studies [12], [13], [14], [72], [73] where the RR limit was used instead of a threshold limit.

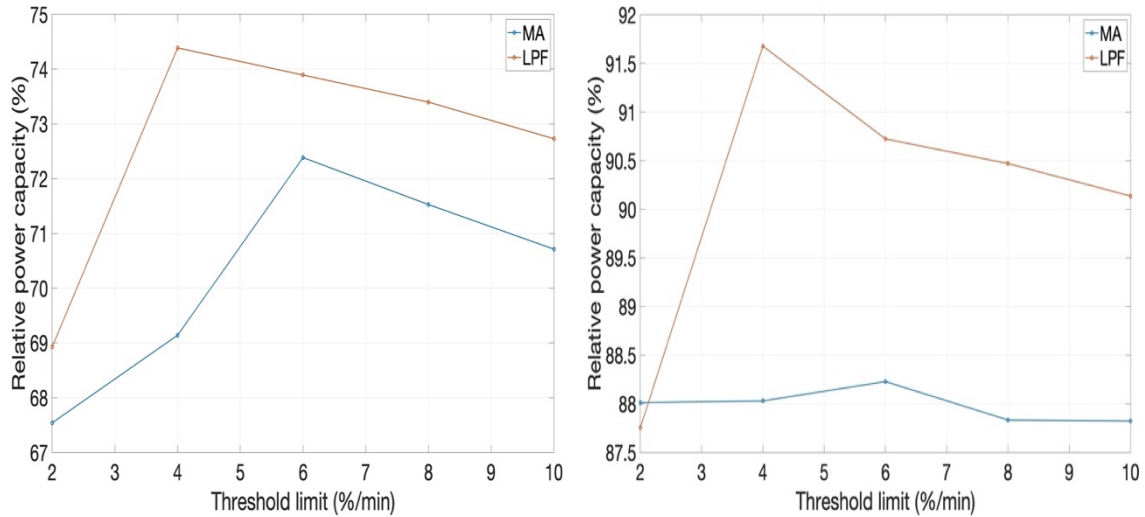


Figure 5.4. Required relative power capacities of the ESSs as a function of threshold limits for 11.06.2021 (left) and 15.06.2021 (right).

In Figure 5.4, for both days, it is seen that the required relative power capacity increases to 4 %/min and 6 %/min, and after that, the required relative power capacity decreases for the LPF and MA, respectively. For day 11.06.2021, the required relative power capacity at the threshold limit of 10 %/min is higher than the required relative power capacity at the threshold limit of 2 %/min for both MA and LPF. For day 15.06.2021, the required relative power capacity at 10 %/min is higher than the required relative power capacity at 2 %/min for MA. However, the required relative power capacity at 10 %/min is lower than the required relative power capacity at 2 %/min for LPF. This means that the required relative power capacity is inconsistent and does not decrease with the increasing threshold limit. The possible reasons for showing the dissimilarities with the refs. [12], [13], [72], [73] could be the use of different controlling strategies like RR-based and SOC control methods instead of MA and LPF with threshold limits. Also, refs. [12], [13], [73] used the modeled PV power data instead of measured data. This means that the increase in the threshold limit has less effect on the relative power capacity of the ESS because the moving clouds produce power ramps for PV power plants that are typically far faster than even the strictest threshold limits [25].

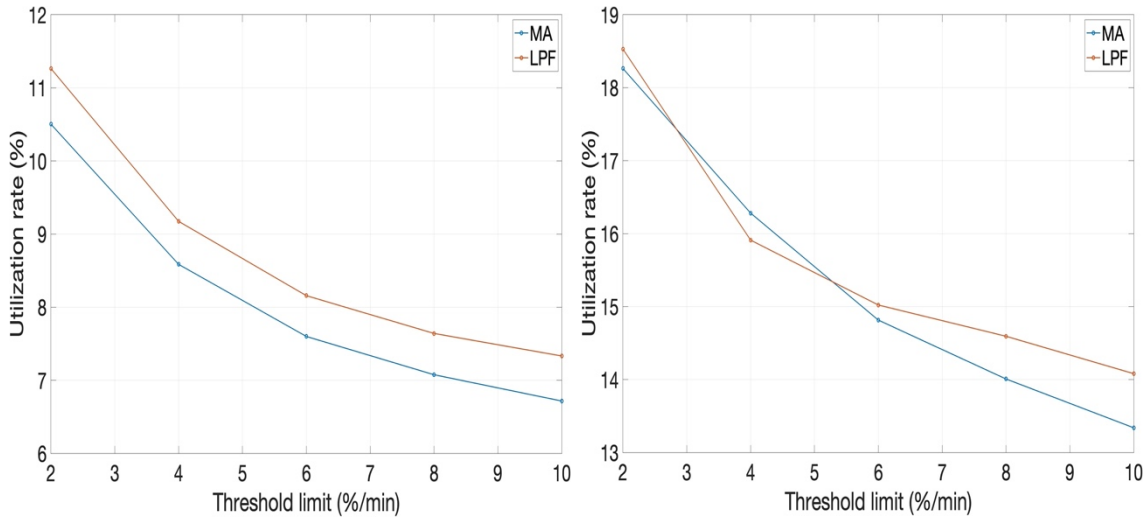


Figure 5.5. Utilization rates of the ESSs as a function of threshold limits for 11.06.2021 (left) and 15.06.2021 (right).

In Figure 5.5, for day 11.06 2021, it is seen that the utilization rate decreases as the threshold limit increases. The results show similarities with the refs. [14], [73] where the RR limit was used instead of a threshold limit.

5.3 Sizing of the ESSs with three different time constants

In this subchapter, the size of the ESSs is identified by varying the time constants of the MA and LPF. The time constant ranges from 100 to 1000 s for MA and from 10 to 100 s for LPF. In this analysis, three different types of time constants are considered. The initial one has shorter time constants (100 s for the MA and 10 s for the LPF). The second one has intermediate time constants (550 s for MA and 55 s for LPF). The final one has longer time constants (1000 s for MA and 100 s for LPF). Finally, the results obtained with these time constants are compared with each other.

In this example, the threshold limit of 6 %/min has been chosen. Tables 5.5 and 5.6 present the results of the sizing of the ESS for days 11.06.2021 and 15.06.2021, respectively. The sizing quantities like energy capacity, charging and discharging power capacity, relative energy and power capacity, energy charged and discharged, energy fed to the grid, and share of energy cycled through the ESS, including the used time constants and the highest observed RR of the grid power, are shown in Tables 5.5 and 5.6.

Table 5.5. Three different time constants, the highest observed power ramp rates, and the sizing of the ESS with the MA and LPF for 11.06.2021.

Control Strategies	MA			LPF		
Threshold limit (%/min)	6			6		
Time constant (s)	100	550	1000	10	55	100
Highest observed RR (%/min)	5.9990	5.9990	5.9990	5.9997	5.9991	5.999
Energy capacity (kWh)	0.4128	0.3188	0.4258	0.4005	0.4025	0.4056
Relative energy capacity (h)	0.1278	0.0987	0.1318	0.124	0.1246	0.1256
Charging power capacity (kW)	2.4203	2.3380	2.3380	2.3505	2.3670	2.3722
Discharging power capacity (kW)	2.0368	2.0449	2.0481	2.0952	2.1	2.1015
Relative power capacity (%)	74.9304	72.3851	72.3851	72.7724	73.2804	73.4435
Energy charged (kWh)	1.1603	1.3581	1.2737	0.9575	0.9665	0.9766
Energy discharged (kWh)	1.5945	1.3929	1.4866	1.5838	1.5839	1.583
Energy fed to the grid (kWh)	19.3835	18.984	19.1622	19.5756	19.5666	19.5557
Share of energy cycled through the ESS (%)	8.2263	7.337	7.7579	8.0909	8.0949	8.0947

In Table 5.5, for MA, the relative energy capacity for the longer time constant is 3.13 % and 33.54 % higher than that of the shorter and intermediate time constants. The relative power capacity of the shorter time constant is only 3.52 % higher than that of the intermediate and longer time constants. The utilization rate of the ESS for shorter time constants is only 12.12 % and 6.04 % higher than that of the intermediate and longer time constants. However, in the case of LPF, the relative energy capacity, relative power capacity, and utilization rate are almost the same for shorter, intermediate, and longer time constants.

Figure 5.6 shows the smoothed grid and PV output power with three different time constants using the MA strategy for days 11.06.2021 and 15.06.2021.

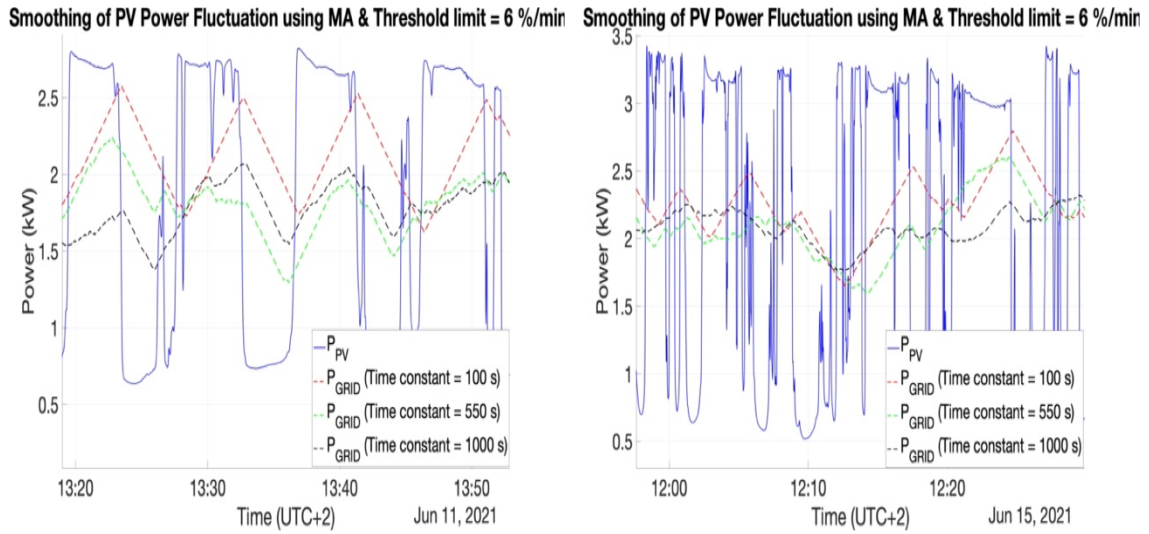


Figure 5.6. Power of the 3.23 kW PV string and smoothed grid power with 3 different time constants using MA strategy for 11.06.2021 and 15.06.2021.

In Figure 5.6, it is seen that the higher is the time constant, the stronger is the smoothing of the PV power and the reduction in the amplitude of the grid power oscillation. This result with the implementation of the threshold limit shows similar outcomes to the refs. [74], [75], where the threshold limit was not used.

Table 5.6. Iterated three different time constants, the highest observed power ramp rates, and the sizing of the ESS with the MA and LPF for 15.06.2021.

Control Strategies	MA			LPF		
Threshold limit (%/min)	6			6		
Time constant (s)	100	550	1000	10	55	100
Highest observed RR (%/min)	5.9976	5.9982	5.9994	5.9998	5.9991	5.9976
Energy capacity (kWh)	0.4541	0.3821	0.5176	0.6162	0.6082	0.604
Relative energy capacity (h)	0.1406	0.1183	0.1602	0.1908	0.1883	0.187
Charging power capacity (kW)	2.9407	2.8498	2.8814	2.8597	2.8801	2.896
Discharging power capacity (kW)	2.4777	2.3202	2.2148	2.6021	2.609	2.6034
Relative power capacity (%)	91.0428	88.2279	89.2063	88.5358	89.1673	89.6609
Energy charged (kWh)	2.0460	2.2992	2.3493	1.6818	1.7312	1.7546
Energy discharged (kWh)	2.2851	2.2042	2.1697	2.4263	2.3954	2.3901
Energy fed to the grid (kWh)	15.1488	14.8147	14.7301	15.6541	15.5739	15.5452
Share of energy cycled through the ESS (%)	15.0841	14.8787	14.7299	15.4993	15.3809	15.3752

In Table 5.6, for MA, the relative energy capacity for the longer time constant is 13.94 % and 35.42 % higher than that of the shorter and intermediate time constants. The relative power capacity of the shorter time constant is only 3.19 % and 2.06 % higher than that of the intermediate and longer time constants. The utilization rate of the ESS for a shorter time constant is only 1.38 % and 1.14 % higher than that of the intermediate and longer time constants. However, in the case of LPF, the relative energy capacity, relative power capacity, and utilization rate are almost the same for shorter, intermediate, and longer time constants.

In general, for both Tables 5.5 and 5.6, the results do not show similarities with the findings of [75], [76], except for LPF, where the relative energy capacity on June 11, 2021, and the relative power capacity on both days increase as the time constants increase. Also, there are no significant differences in the relative energy capacity and relative power capacity in LPF. The possible reasons could be the implementation of smoothing strategies only when the RR of the PV output power is above or equal to the threshold limit. Also, the utilization rate was not calculated in earlier studies for the comparison of the utilization rate of the ESS with different time constants.

5.4 Discussion

This section outlines the findings and implications derived from the simulation results. The goal of this thesis was to analyze the impact of various smoothing strategies, alongside the presence or absence of different threshold limits, and different time constants on the sizing of ESSs.

In subchapter 5.1, an analysis of the sizing of ESSs between MA and LPF revealed that LPF exhibited notably higher relative energy capacity compared to MA for both days. However, there were negligible variances in the relative charging and discharging power capacity and the utilization rate of the ESSs. Additionally, LPF showed a tendency to slightly over-smooth the PV output power in comparison to MA. The technical constraints that affect the sizing of the ESSs for MA and LPF are the size of the PV power plant, modeled PV power data instead of measured data, and sampling frequency.

In subchapter 5.2, it was observed that increasing the threshold limit led to a decrease in the required relative energy capacity and utilization rate of the ESSs for both MA and LPF on both days. However, there was inconsistency in the relative power capacity, as it did not decrease with the increasing threshold limit for both MA and LPF. When comparing the sizing of the ESS with and without using the threshold limit, it was found that the required relative energy capacity of the ESS without the threshold limit was lower compared to all the threshold limits. In general, for both days and MA and LPF, the required relative power capacity of the ESS without the threshold limit was lower compared

to those with the threshold limits. On June 11, 2021, for MA, it was observed that the utilization rate of the ESS without the threshold limit was lower compared to those below the threshold limit (≤ 2 %/min) but higher compared to those above the threshold limit (> 2 %/min). For LPF, it was observed that the utilization rate of the ESS without the threshold limit was lower compared to those below the threshold limit (≤ 4 %/min) but higher compared to those above the threshold limit (> 4 %/min). Similarly, on June 15, 2021, the utilization rate of the ESS without the threshold limit was lower compared to those below the threshold limit (≤ 2 %/min) for both MA and LPF. However, it was higher compared to those above the threshold limit (> 2 %/min). Additionally, it was noted that the highest observed RR in the grid power closely matched or equaled the applied threshold limits for both MA and LPF.

In subchapter 5.3, an analysis of MA revealed that, for both days, the required relative energy capacity was higher with longer time constants compared to shorter and intermediate ones. However, the required relative power capacity for shorter time constants slightly surpassed that of the intermediate and longer ones. On both days, the utilization rate for shorter time constants was higher than for intermediate and longer time constants. Nonetheless, LPF exhibited similar relative energy capacity, relative power capacity, and utilization rates across different time constants. Increasing the time constant enhanced the smoothing of the PV power, However, increasing the time constant did not increase the size of the ESS compared to the refs. [75], [76]. This discrepancy may originate from the utilization of smoothing strategies only when the RR of the PV output power reaches or exceeds the threshold limit.

6 Conclusion

This chapter discusses the challenges encountered, provides a summary of the findings, and outlines potential future research directions for this thesis. The global expansion of renewable energy sources, such as solar and wind power plants, is rapidly increasing. However, these sources exhibit intermittent and unpredictable characteristics, leading to rapid fluctuations in output power. As a result, integrating these resources into the power grid presents challenges such as power instability and fluctuations in voltage and frequency. To address these issues, one solution is the incorporation of ESSs to mitigate the rapid power fluctuations in PV power systems.

The thesis aimed to determine the sizing of ESSs through various smoothing strategies, with and without threshold limits, and different time constants. Furthermore, it aimed to analyze their impact on ESS sizing and utilization rates. It introduced novel approaches by implementing smoothing strategies like MA and LPF with threshold limits, where the algorithm was activated only when the RR in the power fed to the grid exceeded a specified threshold. The study relied solely on simulation work conducted using MATLAB to control PV output power fluctuations and estimate ESS sizing. Measurements were conducted at the Finnish Solar PV Power Station Research Plant at Tampere University, specifically on June 11 and 15, 2021.

The primary challenge encountered during the simulation was managing the high RR in the grid power, which exceeded the specified threshold limit when toggling the algorithm on or off. Despite applying the threshold limit to smooth the PV output power, the toggling of the algorithm resulted in excessively high RR in the grid power. To address this issue, the RR in the grid power was adjusted back to the specified threshold limit by gradually increasing or decreasing the previous grid power close to the allowed threshold limit. Additionally, previous studies have not explored the implementation of the threshold limit for analyzing and comparing the sizing of ESSs, making it a novel aspect of this research.

The comparative analysis between MA and LPF revealed that the primary factor influencing the size of the ESS was its relative energy capacity. MA emerged as the superior choice for minimizing relative energy capacity. Specifically, on the dates June 11, 2021, and June 15, 2021, the required relative energy capacity for LPF was 67.97 % and 83.42 % higher, respectively, compared to MA. It was found that the differences in required relative charging and discharging power capacity, as well as the utilization rate of the ESS, between MA and LPF, were minimal. These findings exhibit similarities with previous research in the field.

In the comparison of ESS sizing across various threshold limits, it was noted that the required relative energy capacity and utilization rate decreased with higher threshold limits, which shows similarities with prior research. The required relative energy capacity was highest at 2 %/min and lowest at 10 %/min. However, the required relative power capacity exhibited a nonlinear increase with higher threshold limits, which shows dissimilarities with earlier findings. This divergence can be attributed to the implementation of novel smoothing strategies utilizing the threshold limit. Similarly, when comparing ESS sizing with and without the threshold limit, results indicated that the utilization rate without the threshold limit was lower than those below the threshold limit (≤ 2 %/min and ≤ 4 %/min). Conversely, the required relative energy without the threshold limit was higher than those above the threshold limit (> 2 %/min and > 4 %/min). Additionally, it appears advantageous to utilize ESSs without the threshold limit to reduce relative energy and relative power capacity.

In the analysis comparing the sizing of the ESS across various time constants, in general, it was evident that relative energy capacity played a more significant role in determining ESS sizing than relative power capacity and utilization rate for MA. Conversely, for LPF, varying time constants had minimal impact on relative energy capacity, relative power capacity, and utilization rate.

In future studies, expanding the simulation to incorporate a larger PV plant instead of a fixed small one would enable analysis of how the size of the PV plant influences the sizing of ESSs and its practical applicability. Additionally, incorporating the RR-based control method would be advantageous for PV power RR exceeding 10 %/min. For RR below 10 %/min, the same strategies involving MA and LPF can be applied to influence the sizing and utilization rate of the ESS. Moreover, it would be beneficial to include losses in the inverter and other components, as well as energy losses within the ESS, within the system analysis.

References

- [1] IEA, 'Net Zero by 2050', p. 224, Oct. 2021.
- [2] M. H. Albadi, 'SOLAR PV POWER INTERMITTENCY AND ITS IMPACTS ON POWER SYSTEMS-AN OVERVIEW.', *Journal of Engineering Research*, vol. 16, no. 2, 2019.
- [3] J. Marcos, L. Marroyo, E. Lorenzo, D. Alvira, and E. Izco, 'Power output fluctuations in large scale PV plants: one year observations with one second resolution and a derived analytic model', *Progress in Photovoltaics: Research and Applications*, vol. 19, no. 2, 2011.
- [4] M. S. Alam, F. S. Al-Ismail, and M. A. Abido, 'PV/wind-integrated low-inertia system frequency control: PSO-optimized fractional-order PI-based SMES approach', *Sustainability*, vol. 13, no. 14, 2021.
- [5] O. Gandhi, D. S. Kumar, C. D. Rodríguez-Gallegos, and D. Srinivasan, 'Review of power system impacts at high PV penetration Part I: Factors limiting PV penetration', *Solar Energy*, vol. 210, 2020.
- [6] Y. G. Landera, O. C. Zevallos, R. C. Neto, J. F. da C. Castro, and F. A. Neves, 'A Review of Grid Connection Requirements for Photovoltaic Power Plants', *Energies*, vol. 16, no. 5, 2023.
- [7] V. Gevorgian and S. Booth, 'Review of PREPA technical requirements for interconnecting wind and solar generation', National Renewable Energy Lab.(NREL), Golden, CO (United States), 2013.
- [8] Energinet, 'Technical Regulation 3.2.2 for PV Power Plants Above 11 kW', p. 111, 2016.
- [9] IEA, 'How Rapidly Will the Global Electricity Storage Market Grow by 2026?', Dec. 2021, [Online]. Available: <https://www.iea.org/articles/how-rapidly-will-the-global-electricity-storage-market-grow-by-2026>
- [10] European Commission, 'Recommendations on energy storage', [Online]. Available: https://energy.ec.europa.eu/topics/research-and-technology/energy-storage/recommendations-energy-storage_en
- [11] J. Marcos, I. De la Parra, M. García, and L. Marroyo, 'Control strategies to smooth short-term power fluctuations in large photovoltaic plants using battery storage systems', *Energies*, vol. 7, no. 10, 2014.
- [12] J. Schnabel and S. Valkealahti, 'Compensation of PV generator output power fluctuations with energy storage systems', in *European Photovoltaic Solar Energy Conference*, 2015.
- [13] J. Schnabel and S. Valkealahti, 'Energy storage requirements for PV power ramp rate control in Northern Europe', *International Journal of Photoenergy*, vol. 2016, 2016.
- [14] K. Lappalainen and S. Valkealahti, 'Sizing of energy storage systems for ramp rate control of photovoltaic strings', *Renewable Energy*, vol. 196, 2022.
- [15] D. Zhang *et al.*, 'Control strategy and optimal configuration of energy storage system for smoothing short-term fluctuation of PV power', *Sustainable Energy Technologies and Assessments*, vol. 45, 2021.
- [16] S. Sukumar, M. Marsadek, K. R. Agileswari, and H. Mokhlis, 'Ramp-rate control smoothing methods to control output power fluctuations from solar photovoltaic (PV) sources—A review', *Journal of energy storage*, vol. 20, 2018.
- [17] International Energy Agency (IEA), 'Photovoltaic Power System Program (PVPS) Annual Report', p. 126, 2020.
- [18] H. Häberlin, *Photovoltaics: system design and practice*. John Wiley & Sons, 2012.

- [19] P. Devices—Part, ‘3: Measurement principles for terrestrial photovoltaic (PV) solar devices with reference spectral irradiance data’, *International Organization for Standardization, ISO Central Secretariat, Geneva, Switzerland, ISO/IEC*, 2008.
- [20] T. H. Al-theanat and M. A. Lpizra, ‘The Effects of Intermittent Solar Radiation in Off-grid Solar Power System’, 2015.
- [21] J. L. Gray, ‘The physics of the solar cell’, *Handbook of photovoltaic science and engineering*, vol. 2, 2011.
- [22] Office of Energy Efficiency & Renewable Energy, ‘Crystalline Silicon Photovoltaics Research’, 2023, [Online]. Available: <https://www.energy.gov/eere/solar/crystalline-silicon-photovoltaics-research>
- [23] NREL, ‘Best Research-Cell Efficiency Chart’, 2024, [Online]. Available: <https://www.nrel.gov/pv/cell-efficiency.html>
- [24] R. Perez, P. Lauret, M. Perez, M. David, T. E. Hoff, and S. Kivalov, ‘Solar resource variability’, *Wind Field and Solar Radiation Characterization and Forecasting: A Numerical Approach for Complex Terrain*, pp. 149–170, 2018.
- [25] K. Lappalainen and S. Valkealahti, ‘Experimental study of the maximum power point characteristics of partially shaded photovoltaic strings’, *Applied Energy*, vol. 301, 2021.
- [26] M. Järvelä, K. Lappalainen, and S. Valkealahti, ‘Characteristics of the cloud enhancement phenomenon and PV power plants’, *Solar Energy*, vol. 196, 2020.
- [27] Y. Ding, Y. Li, C. Liu, and Z. Sun, ‘Solar electrical energy storage’, in *Solar Energy Storage*, Elsevier, 2015, pp. 7–25.
- [28] A. Sangwongwanich, Y. Yang, and F. Blaabjerg, ‘A cost-effective power ramp-rate control strategy for single-phase two-stage grid-connected photovoltaic systems’, in *2016 IEEE Energy Conversion Congress and Exposition (ECCE)*, IEEE, 2016, pp. 1–7.
- [29] W. A. Omran, M. Kazerani, and M. M. A. Salama, ‘Investigation of methods for reduction of power fluctuations generated from large grid-connected photovoltaic systems’, *IEEE Transactions on Energy Conversion*, vol. 26, no. 1, 2010.
- [30] N. Ina, S. Yanagawa, T. Kato, and Y. Suzuoki, ‘Smoothing of PV system output by tuning MPPT control’, *Electrical Engineering in Japan*, vol. 152, no. 2, 2005.
- [31] J. Chen, J. Li, Y. Zhang, G. Bao, X. Ge, and P. Li, ‘A hierarchical optimal operation strategy of hybrid energy storage system in distribution networks with high photovoltaic penetration’, *Energies*, vol. 11, no. 2, 2018.
- [32] S. O. Amrouche, D. Rekioua, T. Rekioua, and S. Bacha, ‘Overview of energy storage in renewable energy systems’, *International journal of hydrogen energy*, vol. 41, no. 45, 2016.
- [33] F.-B. Wu, B. Yang, and J.-L. Ye, *Grid-scale energy storage systems and applications*. Academic Press, 2019.
- [34] R. A. Huggins and R. A. Huggins, *Energy storage: fundamentals, materials and applications*. Springer, 2016.
- [35] A. Rufer, *Energy storage: systems and components*. CRC Press, 2017.
- [36] H. Chen, T. N. Cong, W. Yang, C. Tan, Y. Li, and Y. Ding, ‘Progress in electrical energy storage system: A critical review’, *Progress in natural science*, vol. 19, no. 3, 2009.
- [37] C. Brivio, S. Mandelli, and M. Merlo, ‘Battery energy storage system for primary control reserve and energy arbitrage’, *Sustainable Energy, Grids and Networks*, vol. 6, 2016.
- [38] B. M. Weedy, B. J. Cory, N. Jenkins, J. B. Ekanayake, and G. Strbac, *Electric power systems*. John Wiley & Sons, 2012.

- [39] S. Eftekharnjad, V. Vittal, G. T. Heydt, B. Keel, and J. Loehr, 'Impact of increased penetration of photovoltaic generation on power systems', *IEEE transactions on power systems*, vol. 28, no. 2, 2012.
- [40] M. S. Alam, F. S. Al-Ismael, A. Salem, and M. A. Abido, 'High-level penetration of renewable energy sources into grid utility: Challenges and solutions', *IEEE Access*, vol. 8, 2020.
- [41] M. G. Molina, 'Dynamic modelling and control design of advanced energy storage for power system applications', *Dynamic Modelling*, vol. 300, 2010.
- [42] I. E. Commission, 'Electrical energy storage', (*No Title*), 2011.
- [43] A. Evans, V. Strezov, and T. J. Evans, 'Assessment of utility energy storage options for increased renewable energy penetration', *Renewable and sustainable energy reviews*, vol. 16, no. 6, 2012.
- [44] H. Zhao, Q. Wu, S. Hu, H. Xu, and C. N. Rasmussen, 'Review of energy storage system for wind power integration support', *Applied energy*, vol. 137, 2015.
- [45] X. Luo, J. Wang, M. Dooner, and J. Clarke, 'Overview of current development in electrical energy storage technologies and the application potential in power system operation', *Applied energy*, vol. 137, 2015.
- [46] J. Intrator, *2020 Strategic Analysis of Energy Storage in California: Final Project Report*. California Energy Commission, 2011.
- [47] A. R. LACAL, N. FITZGERALD, and P. LEAHY, 'Pumped-hydro Energy Storage: Potential for Transformation from Single Dams'.
- [48] M. Dooner and J. Wang, 'Compressed-air energy storage', in *Future Energy*, Elsevier, 2020.
- [49] Y. Ding, Y. Li, C. Liu, and Z. Sun, 'Solar electrical energy storage', in *Solar Energy Storage*, Elsevier, 2015, pp. 7–25.
- [50] Z. Long and Q. Zhiping, 'Review of flywheel energy storage system', in *Proceedings of ISES World Congress 2007 (Vol. I–Vol. V) Solar Energy and Human Settlement*, Springer, 2009.
- [51] R. Peña-Alzola, R. Sebastián, J. Quesada, and A. Colmenar, 'Review of flywheel based energy storage systems', in *2011 International Conference on Power Engineering, Energy and Electrical Drives*, IEEE, 2011, pp. 1–6.
- [52] I. Hadjipaschalis, A. Poullikkas, and V. Efthimiou, 'Overview of current and future energy storage technologies for electric power applications', *Renewable and sustainable energy reviews*, vol. 13, no. 6–7, 2009.
- [53] F. Díaz-González, A. Sumper, O. Gomis-Bellmunt, and R. Villafáfila-Robles, 'A review of energy storage technologies for wind power applications', *Renewable and sustainable energy reviews*, vol. 16, no. 4, 2012.
- [54] A. Du Pasquier, I. Plitz, S. Menocal, and G. Amatucci, 'A comparative study of Li-ion battery, supercapacitor and nonaqueous asymmetric hybrid devices for automotive applications', *Journal of power sources*, vol. 115, no. 1, pp. 171–178, 2003.
- [55] M. H. Ali, B. Wu, and R. A. Dougal, 'An overview of SMES applications in power and energy systems', *IEEE transactions on sustainable energy*, vol. 1, no. 1, 2010.
- [56] W. Yuan, *Second-generation high-temperature superconducting coils and their applications for energy storage*. Springer Science & Business Media, 2011.
- [57] S. Mekhilef, R. Saidur, and A. Safari, 'Comparative study of different fuel cell technologies', *Renewable and Sustainable Energy Reviews*, vol. 16, no. 1, 2012.
- [58] S. Styring, 'Solar fuels: vision and concepts', *Ambio*, vol. 41, no. Suppl 2, pp. 156–162, 2012.

- [59] M. Pagliaro, A. G. Konstandopoulos, R. Ciriminna, and G. Palmisano, 'Solar hydrogen: fuel of the near future', *Energy & Environmental Science*, vol. 3, no. 3, pp. 279–287, 2010.
- [60] A. Steinfeld, 'Solar hydrogen production via a two-step water-splitting thermochemical cycle based on Zn/ZnO redox reactions', *International journal of hydrogen energy*, vol. 27, no. 6, pp. 611–619, 2002.
- [61] A. Sharma, V. V. Tyagi, C. R. Chen, and D. Buddhi, 'Review on thermal energy storage with phase change materials and applications', *Renewable and Sustainable energy reviews*, vol. 13, no. 2, pp. 318–345, 2009.
- [62] D. Zhou, C.-Y. Zhao, and Y. Tian, 'Review on thermal energy storage with phase change materials (PCMs) in building applications', *Applied energy*, vol. 92, pp. 593–605, 2012.
- [63] H. Ibrahim, A. Ilinca, and J. Perron, 'Energy storage systems—Characteristics and comparisons', *Renewable and sustainable energy reviews*, vol. 12, no. 5, pp. 1221–1250, 2008.
- [64] N. Altin, 'Energy storage systems and power system stability', in *2016 International Smart Grid Workshop and Certificate Program (ISGWCP)*, IEEE, 2016, pp. 1–7.
- [65] G. Wang, M. Ciobotaru, and V. G. Agelidis, 'Power smoothing of large solar PV plant using hybrid energy storage', *IEEE Transactions on Sustainable Energy*, vol. 5, no. 3, 2014.
- [66] M. Talvi, 'SIZING OF ENERGY STORAGE SYSTEMS FOR PHOTOVOLTAIC–WIND POWER PLANTS', 2023.
- [67] M. Talvi and K. Lappalainen, 'Effects of Control Strategy on Sizing of Energy Storage Systems for PV-Wind Power Plants', in *European Photovoltaic Solar Energy Conference and Exhibition, EU PVSEC*, 2023.
- [68] L. Al-Ghussain, O. Taylan, and D. K. Baker, 'An investigation of optimum PV and wind energy system capacities for alternate short and long-term energy storage sizing methodologies', *International Journal of Energy Research*, vol. 43, no. 1, 2019.
- [69] A. Al-Shereiqi, A. Al-Hinai, M. Albadi, and R. Al-Abri, 'Optimal sizing of hybrid wind-solar power systems to suppress output fluctuation', *Energies*, vol. 14, no. 17, 2021.
- [70] N. Zhang, N.-C. Yang, and J.-H. Liu, 'Optimal sizing of PV/Wind/Battery hybrid microgrids considering lifetime of battery banks', *Energies*, vol. 14, no. 20, 2021.
- [71] D. Torres Lobera, A. Mäki, J. Huusari, K. Lappalainen, T. Suntio, and S. Valkealahti, 'Operation of TUT solar PV power station research plant under partial shading caused by snow and buildings', *International Journal of Photoenergy*, vol. 2013, 2013.
- [72] J. Marcos, O. Storkel, L. Marroyo, M. Garcia, and E. Lorenzo, 'Storage requirements for PV power ramp-rate control', *Solar Energy*, vol. 99, 2014.
- [73] M. Talvi, T. Roinila, and K. Lappalainen, 'Effects of Ramp Rate Limit on Sizing of Energy Storage Systems for PV, Wind and PV–Wind Power Plants', *Energies*, vol. 16, 2023.
- [74] J. Martins, S. Spataru, D. Sera, D.-I. Stroe, and A. Lashab, 'Comparative study of ramp-rate control algorithms for PV with energy storage systems', *Energies*, vol. 12, no. 7, 2019.
- [75] A. A. Abdalla and M. Khalid, 'Smoothing methodologies for photovoltaic power fluctuations', in *2019 8th International Conference on Renewable Energy Research and Applications (ICRERA)*, IEEE, 2019.

- [76] S. Sukumar, H. Mokhlis, S. Mekhilef, M. Karimi, and S. Raza, 'Ramp-rate control approach based on dynamic smoothing parameter to mitigate solar PV output fluctuations', *International Journal of Electrical Power & Energy Systems*, vol. 96, 2018.

Appendix 1: MA based control algorithm with threshold limit

The provided MATLAB code implements a MA based control algorithm with a threshold limit for smoothing and determining the sizing of ESSs. It begins by loading, extracting, and initializing the necessary variables for computation. The loop section governs the output of PV power to the grid based on the RR. When the RR exceeds or equals the threshold limit, the MA algorithm becomes active; otherwise, it remains inactive. Subsequently, the code computes the power and energy capacity of the ESSs. Finally, it evaluates the maximum RR in the grid power and calculates the sizing requirements for the ESSs.

```
% Load data
data = load('Data_2021-06-11.mat');

% Extract variables
PV_power = data.Data.P_PV;
date_time = data.Data.time;

% ESS algorithm parameters
T_s = 1; % Sampling time in sec (1 Hz)
P_NOMINAL = 3230; % W
RR_Threshold = 10; % Vary the RR threshold
P_threshold = (P_NOMINAL * RR_Threshold) / (100 * 60); % RR threshold
converted to W/sec

% Initializing some variables
Pgrid = zeros(length(date_time), 1);
PESS = zeros(length(date_time), 1);
EESS = zeros(length(date_time), 1);
Pgrid(1) = PV_power(1);
EESS(1) = 0;
PESS(1) = 0;
Eenergycharged = 0;
Eenergydischarged = 0;
timeESScharged = 0;
timeESSdischarged = 0;
Egrid = 0;

% Extract the time from the data
datetime_data = datetime(date_time);
% Calculate time differences in seconds
time_diff_seconds = seconds(diff(datetime_data));

% Calculate the rate of change of PV power (W/sec)
P_RR = abs(diff(PV_power) ./ time_diff_seconds);
T_c = 566; % Time constant in sec

%% ESS algorithm loop
for i = 2:length(date_time)
    % Check if PV power fluctuation is greater than a threshold limit
    if P_RR(i-1) >= P_threshold
        % Use energy storage with a simple moving average method
        Pgrid(i) = sum(PV_power(max(1, i - T_c + 1):i)) / T_c;
        if abs(Pgrid(i) - Pgrid(i-1)) / time_diff_seconds(i-1) >=
P_threshold
```

```
        Pgrid(i) = Pgrid(i-1) + sign(Pgrid(i) - Pgrid(i-1)) * 0.99
* P_threshold * time_diff_seconds(i-1);
    end
    % Adjust energy storage
    PESS(i) = PV_power(i) - Pgrid(i);
    EESS(i) = EESS(i - 1) + PESS(i) * T_s;
    Egrid = Egrid + Pgrid(i) * T_s;

    if PESS(i) > 0
        Energycharged = Energycharged + PESS(i) * T_s;
        timeESScharged = timeESScharged + T_s;
    elseif PESS(i) < 0
        Energydischarged = Energydischarged + abs(PESS(i)) *
T_s;
        timeESSdischarged = timeESSdischarged + T_s;
    end
    else
    % Do not use energy storage
    Pgrid(i) = PV_power(i);
    % Check if the difference in consecutive Pgrid values is below
the threshold
    if abs(Pgrid(i) - Pgrid(i-1)) / time_diff_seconds(i-1) >=
P_threshold
        Pgrid(i) = Pgrid(i-1) + sign(Pgrid(i) - Pgrid(i-1)) * 0.99
* P_threshold * time_diff_seconds(i-1);
        % Adjust energy storage
        PESS(i) = PV_power(i) - Pgrid(i);
        EESS(i) = EESS(i - 1) + PESS(i) * T_s;

        if PESS(i) > 0
            Energycharged = Energycharged + PESS(i) * T_s;
            timeESScharged = timeESScharged + T_s;
        elseif PESS(i) < 0
            Energydischarged = Energydischarged + abs(PESS(i)) *
T_s;
            timeESSdischarged = timeESSdischarged + T_s;
        end
        end
        Egrid = Egrid + Pgrid(i) * T_s;
    end
end

% Calculate the ramp rate of the filtered signal
Pgrid_RR1 = abs(diff(Pgrid) ./ time_diff_seconds); % Ramp rate in
W/sec
% Convert ramp rate to %/min
Pgrid_RR_percent_per_min = ((Pgrid_RR1 * 60) / P_NOMINAL) * 100;

% Find the maximum observed ramp rate
[max_ramp_rate, max_ramp_rate_index] =
max(Pgrid_RR_percent_per_min(2:end));

%% Saving the sizing requirements of the ESS
E_ESS = (max(EESS) + abs(min(EESS)))/(3600*1000);%kWh
P_ESS_charge = max(PESS)/1000; %kW
P_ESS_discharge = min(PESS)/1000; %kW
Relative_energy_ESS = (E_ESS*1000)/ P_NOMINAL; % hours
Relative_power_ESS = (max(abs(PESS)) / P_NOMINAL) * 100; % percentages
Energy_charged = Energycharged/(3600*1000); %kWh
```

```
Energy_discharged = Eenergydischarged/(3600*1000);%kWh  
Energy_grid = Egrid/(3600*1000); %kWh  
Energy_cycled = (Eenergydischarged*100) / Egrid; %percentage  
time_ESS_charged = timeESScharged;  
time_ESS_discharged = timeESSdischarged;
```